DE GRUYTER

Curved and Layered Structures 2024; 11: 20240017

Research Article

Zoa Ambassa* and Ossende Owona Cyprien Felix

FEM for improvement of damage prediction of airfield flexible pavements on soft and stiff subgrade under various heavy load configurations of landing gear of new generation aircraft

https://doi.org/10.1515/cls-2024-0017
received March 21, 2024; accepted September 21, 2024

Abstract: This study establishes the state-of-the-art requirements verification process applied to compute the damage of flexible airfield pavement from new French rational method. Flexible pavement structures with platforms A, B, C, and D, recommended by International Civil Aviation Organization (ICAO), were modelled under static loading of bogies from heavy weight aircrafts A340, B777, and A380 using Cast3M 3D finite element modelling. From the results of these computations, it appears that these structures A, B, C, and D recommended by ICAO are not equivalent from the point of view of mechanical behaviour as claimed by the empirical method for the design of aeronautical bituminous pavements with abacus. The representation of the strain shapes was done with 3D and 2D profiles to improve the quality of response and to clearly identify the critical areas when an aircraft bogie is passing. The four- and six-wheels bogies of the aircraft A380 are more destructive to flexible pavements than the bogies of the other aircrafts tested in this study. The calculation of damage according to the new French rational method for aeronautical flexible pavements revealed that the main damage to these pavements is due to the fatigue of the bituminous layers and not the rutting of subgrade and the unbound granular material layers.

Keywords: flexible pavements, ICAO, Cast3M 3D FEM, static loading, bogies, heavy weight, damage

List of notations

A340	AIRBUS 340
A380-800	AIRBUS 380-800
ACN	aircraft classification number
BB	Aeronautic asphalt concrete
B777-300ER	BOEING 777-300ER
CBR	California Bearing Ratio
FEM	finite element modelling
GAN	The Guide to the Application of Standards
GB	bituminous gravel
GTR	French subgrade classification for transportation geotechnics
ICAO	International Civil Aviation Organization
PCN	pavement classification number
RseR	Rational Equivalent Single Wheel Load
S_N	The dispersion of the results of the fatigue tests on the asphalt concrete described by the standard deviation
S_h	The thickness of the layers made of bituminous binders is variable, with a dispersion that is expressed by the standard deviation S_h
UGM	unbound granular materials
$\varepsilon_{\mathrm{t,T}}$	transverse tensile strain
$\varepsilon_{\mathrm{t,L}}$	longitudinal tensile strain
ε_Z	vertical compressive strains

1 Introduction

The management of airfield pavements includes the determination and control of aircraft loads so that they can be transported safely on the pavement, without causing structural damage to the aircraft or to the pavement. These

---

* **Corresponding author: Zoa Ambassa,** Department of Civil Engineering, Laboratory of Energy Modeling Materials and Methods (E3M), National Higher Polytechnic School of Douala, University of Douala, P.O. Box: 2701, Douala, Cameroon, e-mail: zoa.amabassa@enspd-udo.cm
Ossende Owona Cyprien Felix: Department of Earth Sciences, University of Yaounde 1, P.O. Box: 812, Yaounde, Cameroon

airfield pavements will deteriorate rapidly if subjected to aircraft loads that exceed the structural strength of the pavement [1]. To prevent them from being overloaded and sustaining structural damage, their strength should be assessed and reported so that the aircraft mass should not exceed the strength of the pavement [1–3]. Allowing operations with overloads is a risk that may cause accelerated damage of the structure and reduction in the service life of the pavement. The overloading of pavements can come from excessively heavy loads, or from the rate of application of substantially high loads, or both. Pavements are designed to support a defined load for a predictable number of applications during their lifetime [4]. Therefore, occasional minor overloading is acceptable, with only a limited reduction in expected pavement life, and with relatively little acceleration of pavement deterioration. The evolution of airport traffic and aircraft architecture create new stress conditions, such as multi-peak loading with large strains [5–7]. New generation aircrafts, large carriers, of the A380-800 and B777-300ER type, *e.g.* which are relatively restrictive for flexible pavements, require a detailed analysis of the behaviour of materials under this type of stress and to better quantify the effect of the large amplitudes of stress caused by these aircrafts, which exceed those applied by an heavy weight axle the on road pavement [5–7]. The absence of a complete understanding of the behaviour of materials in the face of these stresses, under different climatic and environmental conditions, sometimes leads to an insufficient or excessive study of the pavement structure, thus proving to be uneconomical.

For decades, the flexible airfield pavements design analyses performed in practice still use International Civil Aviation Organization's (ICAO) empirical California Bearing Ratio (CBR) [4,8], based on Equivalent Single Wheel Load. The issue of pavement compatibility was considered to be fundamental to the programme, especially as the current Aircraft classification number/Pavement classification number (ACN/PCN) method was shown to have reached its limit of reliability with the unpredicted cracks of pavements subject to 6-wheels bogie loads. The finite element method represents a powerful alternative approach for pavement response mechanistic analysis submitted by various load configurations [1,9–11]. Pavement response analysis is accurate, versatile, and requires fewer *a priori* assumptions, especially, regarding the failure mechanism and damage. In this work, we combine the practicality of empirical methods with the technical soundness of mechanistic solutions and use mechanistic analysis, to improve and determine the pavement response to imposed load, then apply "empirical" formulations to determine the development of distress due to the load-induced pavement response. The pavement structures consist of three layers above the subgrade: subbase, base courses, and asphalt surfacing. Only the subbase had a variable thickness depending on the subgrade category and for comparison purposes. The simulation was able to represent main landing gear configurations of various wide bogies: A380, A340, and B777. Up to 22 wheels could be individually loaded up to 32 tons [12,13]. The modelling performed quasi-static comparisons of landing gear configurations. These analyses provided data on the effects of interference when wheels or legs spacing changed, comparisons between various A380, A340, B777 landing gear configurations and with their main competitors. After this stage, another fatigue and rutting analysis was launched to evaluate the structure of crack modes.

The objectives of this study are: 1. to improve the reproduction and displaying the pavement response in 3D view, allowing the identification of critical points depending on the landing gear configuration; 2. to verify whether the four types of pavement subgrade recommended for ICAO for the design airfield pavements are really equivalent from the point of view of mechanical resistance; and 3. to determine the damage mechanisms of pavement structures [14] under high intensity loads and to determine the critical response (most critical layers) for damage.

2 Methodology

The airport flexible pavement modelling would be a representative of all types of subgrades considered by the ACN/PCN method, from very low strength to very high strength. These subgrades are characterized by: subgrade A: CBR = 15; subgrade B: CBR = 10; subgrade C: CBR = 6, and subgrade D: CBR = 3 [4,8].

2.1 General design calculation

The French empirical method for airfield pavement design uses the CBR method, based on "Equivalent Single Wheel" concept [4,8]. The complex landing gear is first converted in an equivalent single wheel thanks to the Boyd and Foster simplified method. The CBR formula, determined by the US Corps of Engineers, allows the calculation of an equivalent thickness of pavement for which the vertical stress produced at the top of the pavement by a single load P at a pressure q applied 10,000 times produces acceptable stress at the subgrade level; this formula, combined with Boyd and Foster transformation allows us to draw design charts for each aircraft. The CBR formula outputs an effective thickness for a homogeneous body constituted by a reference material (unbound gravel, crushed and well graded, with an elastic modulus $E = 500$ MPa). In reality, the pavement is composed of several courses each having different mechanical quality. Equivalent thickness is transformed to real thickness thanks to the concept of coefficient of equivalence, which is different for each type of material.

2.2 Choice of pavement structures

In the aeronautical field, there is a standardization in the design of pavements, as well as their operation, which is a necessity. The runways and aircraft meet specifications that are largely standardized by the recommendations of the ICAO. The thicknesses of the pavement structures corresponding to the categories of subgrade and the reference load A380 are determined from the chart in Figure 1 and given in Tables 1 and 2 below.

For practical reasons, we opted for the same thickness of the treated materials (bituminous layers) in all the structures and we only varied the thickness of the unbound granular materials (UGM) of the subbase layer. The equivalent thicknesses transformed into real thicknesses are given in Table 2.

The mechanical and geometrical characteristics (Figure 2) of the pavement structures selected, according to the subgrade obtained by the ACN/PCN method, are represented in Table 3.

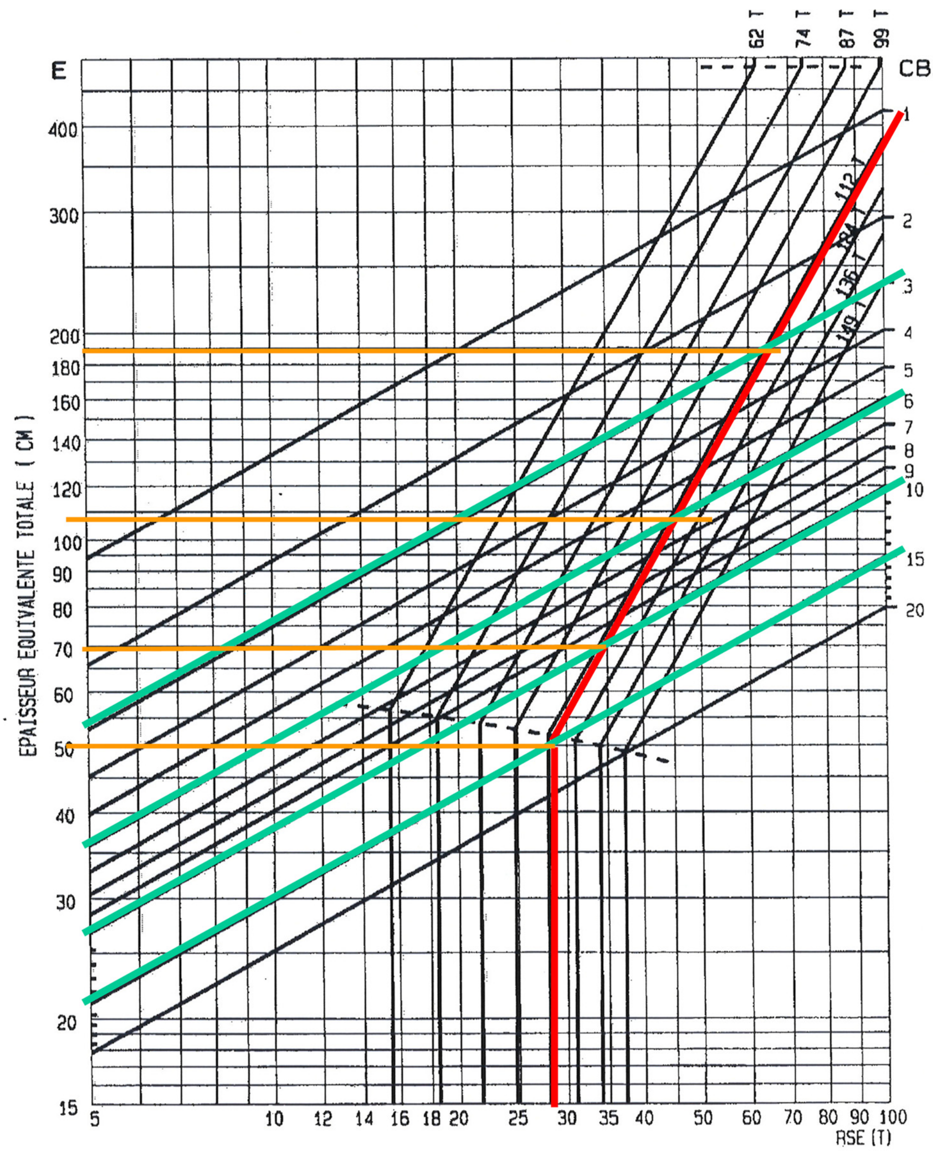

Figure 1: Determination of the thickness of the pavement layers according to the loading and the CBR of the subgrade.

Table 1: Equivalent thicknesses of pavement structures

Equivalent thicknesses of materials (cm)	Structures			
	Type A (CBR = 15)	**Type B (CBR = 10)**	**Type D (CBR = 6)**	**Type D (CBR = 3)**
Total equivalent thicknesses (cm)	50	70	108	190
Minimal equivalent thicknesses of the bituminous materials (cm)	32	36	41	49

For the type A and D structures, we opted for a subbase layer in UGM of 12 and 120 cm, respectively, in order to reduce the number of finite elements and the calculation time on Cast3M [15]. Young's modulus for these four subgrade structures have been assessed experimentally by *in situ* plate tests [12,16,17] for these soils to take into account these subgrades modulus (Table 3) for the numerical modelling.

2.3 Pavement materials specifications

2.3.1 Surface course materials

The course is the aeronautic asphalt concrete (BB) of 8 cm thickness, which is a standardized material (standard NF P 98 131) [18]. The mean value of the *in situ* compaction has to be between 94 and 97%. The specifications required a 0/14 continuous grading with the following characteristics recommended by the GAN [18]:

- Grading: Sand 0/2: about 37%; Aggregate 2/6.3: about 19%; Aggregate 6.3/10: about 42%, and Fines content: about 2%;
- Aggregate classification: BIIIa (standard NF XP P 18 540) [18];
- Bitumen 50/70: about 6.2% (The bitumen content is defined by the French method = bitumen mass/aggregate mass);
- Reference density: 2.40;
- Gyratory shear compacting press test **(standard NF P 98 252) [18]:** percentage of voids for 10 gyrations: >10; % of voids for 60 gyrations: between 4 and 6;
- Duriez test (standard NF P 98 251-1) [18] for water sensitivity measurement: Resistance to compression (dry): >6 MPa; Ratio (wet/dry): >0.8.

Table 2: Actual thicknesses of material Layers

Real thicknesses of each layer		Equivalent thickness
Surface layer: 8 cm of BB		8 × 2 = 16 cm
Base layer: 22 cm of GB		22 × 1.5 = 33 cm
Subbase layer	Type A (CBR = 15): 1 cm	1 cm
	Type B (CBR = 10): 21 cm	21 cm
	Type C (CBR = 6): 59 cm	59 cm
	Type D (CBR = 3): 141 cm	141 cm

2.3.2 Base course materials

The course is divided in two layers of 11 cm thick each of bituminous gravel (GB3). GB3 is a standardized material (standard NF P 98 138). The specifications required a 0/20 continuous grading with the following characteristics recommended by the GAN [18]:

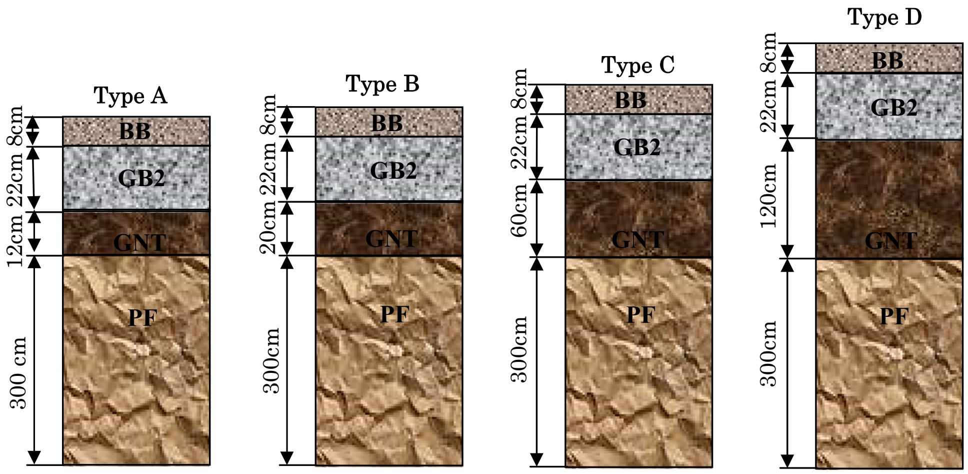

Figure 2: Diagram of pavement structures obtained as a function of the loading and the CBR of the supporting subgrade.

Table 3: Characteristics of the structures analysed

Type	Design	Material	Thickness	Young modulus, E (MPa)	Poisson ratio, ν
			Structure 1		
Type A	Surface layer	BB	80 mm	5,400	0.35
	Base layer	GB2	220 mm	9,300	
	Subbase layer	UGM	120 mm	300	
	Subgrade	CBR = 15	3,000 mm	120	
			Structure 2		
Type B	Surface layer	BB	80 mm	5,400	0.35
	Base layer	GB2	220 mm	9,300	
	Subbase layer	UGM	200 mm	300	
	Subgrade	CBR = 10	3,000 mm	75	
			Structure 3		
Type C	Surface layer	BB	80 mm	5,400	0.35
	Base layer	GB2	220 mm	9,300	
	Subbase layer	UGM	600 mm	300	
	Subgrade	CBR = 6	3,000 mm	40	
			Structure 4		
Type D	Surface layer	BB	80 mm	5,400	0.35
	Base layer	GB2	220 mm	9,300	
	Subbase layer	UGM	1,200 mm	300	
	Subgrade	CBR = 3	3,000 mm	25	

- Grading: Sand 0/2: about 35%; Aggregate 2/6.3: about 13%; Aggregate 6.3/10: about 50%, and Fines content: about 2%;
- Aggregate classification: CIIIa (standard NF XP P 18 540) [18];
- Bitumen 35/50: about 4.5%;
- Reference density: 2.30;
- Gyratory shear compacting press test **(standard NF P 98 252) [18]:** percentage of voids for 10 gyrations: >11; % of voids for 60 gyrations: between 5 and 7;
- Duriez test (standard NF P 98 251-1) [18] for water sensitivity measurement: Resistance to compression (dry): >7 MPa; Ratio (wet/dry): >0.75.

2.3.3 Subbase course materials

A number of successive layers, depending on the final thickness, constitute the course. The material used is UGM. The specifications required a 0/20 graded UGM with the following characteristics [18,19]:

- Aggregate classification: CIIIa (standard NF XP P 18 540) [18], Crushed index: >60%, Moisture: 6%.

2.3.4 Subgrade materials

Subgrades are classified based on the supporting soil according to the recommendations of the ICAO and the GTR (French subgrade classification for transportation geotechnics) [18,19].

3 Finite element modelling (FEM) of pavements on Cast3M

A few FEMs have been made, based on the parameters given in Section 2, with Cast3M code to control the level of strain for each structure loaded in accordance with all landing gear configuration of aircraft analysis. The detailed configuration and geometry of the undercarriages are shown in Figure 3 for A380. Pavement modelling objectives are to optimize the A380, A340, and B777 landing gear configurations and minimize the airport modification cost. In this relation, we were looking for characterized his Main Landing Gear from numerical flexible pavement performed as already existing ones. Nevertheless, it has been necessary to compare the A380 with competitors, such as A340 and B777, on flexible pavement, for a concrete positioning. The three configurations tested during the static modelling made it possible to constitute a very complete database. Figure 3 shows an explanation of the plan view of the landing gear configuration and wheel footprints of the A380-800F parked on the rest area.

3.1 Assumption and simulation data

The multipeak loads will be taken into account in the designing of the pavement structures: these will be the effects of the four-wheels and six-wheels bogies of the landing gears of the heavy carrier aircraft referenced

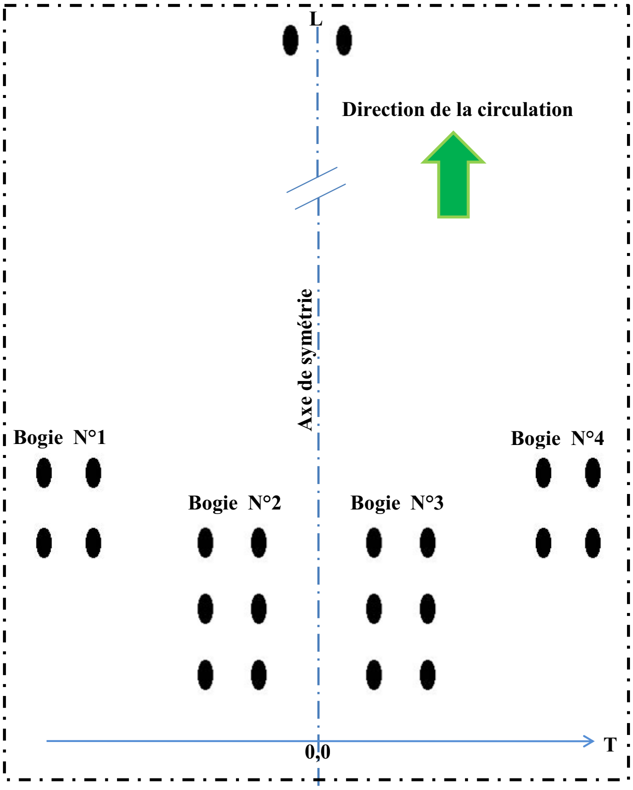

Figure 3: Plan view of the A380-800F four- and six-wheels bogie configuration and wheel footprints parked on the apron.

above, on the aeronautical runways. The specific effects of multipeak loading on the behaviour of these pavements will not only depend on the wheelbase (distance between axles of the same bogie), the track (distance between two wheels of the same axle), and the distance between bogies, but also on the thickness and the rigidity of the pavement layers and on the reversible behaviour law of the materials. All the materials constituting the structures presented have a linear, homogeneous, and isotropic elastic mechanical behaviour with standard parameters. The interfaces between layers of materials are perfectly bonded. In a classic technical analysis of the pavement structure, the approach consists in choosing a mathematical model of this structure and then calculating the response of this mathematical model to the expected loading. Aircraft loads are applied to the pavement by the tires which exert forces on the contact surface. The initial stage of this modelling consists in determining the dimensions of the footprint section at which each wheel of an aircraft bogie exerts a normal pressure depending on the loading, uniformly distributed over the section of its footprint. For 3D models, the tire–pavement contact surface is represented by two semi-circles and a rectangle. It is converted into an equivalent rectangle of area $0.5227L^2$ (Eq. (1)) and width 0.6 L; L being a function of the load (Q) and the contact pressure (p) [20]:

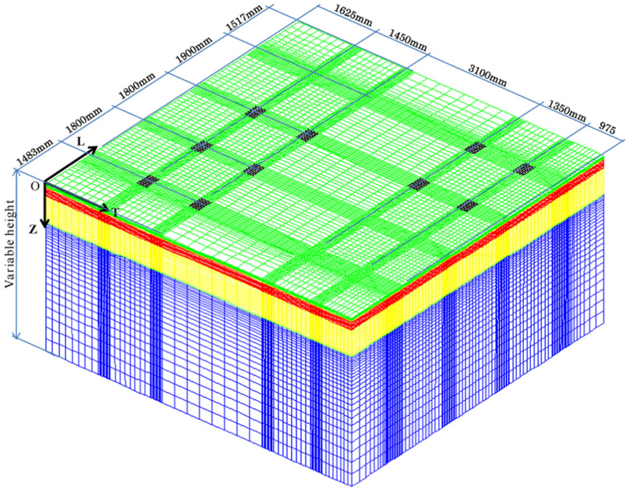

Figure 4: View of Cast3M 3D FEM of pavement on subgrade CBR = 6 under landing gear of A380.

$$L = \left(\frac{Q}{p \times 0.5227}\right)^{\frac{1}{2}}. \tag{1}$$

Given the longitudinal axis of symmetry, only half of the structure is modelled. Figures 4 and 5 present the mesh of the 3D finite element model of the modelled half-carriageway (structures of Type C and D). It is built and used to evaluate the mechanical response of each structure under the effect of the critical loading of the reference aircraft. The thicknesses of the pavement and subgrade layers are along the Z axis and the interfaces between the layers are perfectly bonded. This stage of construction of the 3D finite element model is applied to each of the structures analysed. The construction of the finite element mesh under Cast3M [15] is made using cubic elements with 8 nodes (CUB8) as geometric supports for each layer of material. For example, the mesh of structure D, under load from A380, comprises 546,624 elements and 607,161 nodes. On the area stressed (Figures 4 and 5) by the load, a normal pressure (along the Z axis) is uniformly distributed over a rectangular surface, in order to reproduce the stress of the bogie on the pavement [21]. In Cast3M [15] code, the pavement layers are assembled by massive cubic elements with eight nodes. This element has a variable u_l in each of its eight nodes. Geometric nodes are confused with interpolation nodes. All the details concerning the assembly of this finite element in the 3D modelling were given by Dhatt and Touzot [22]. By using this massive element, stresses, strains, and displacements are obtained at every point of the mesh of the model. The objective of this approach is different from which is sought when the plates and shells elements are used to determine the bending moments in order for the design the structural elements with respect to failure

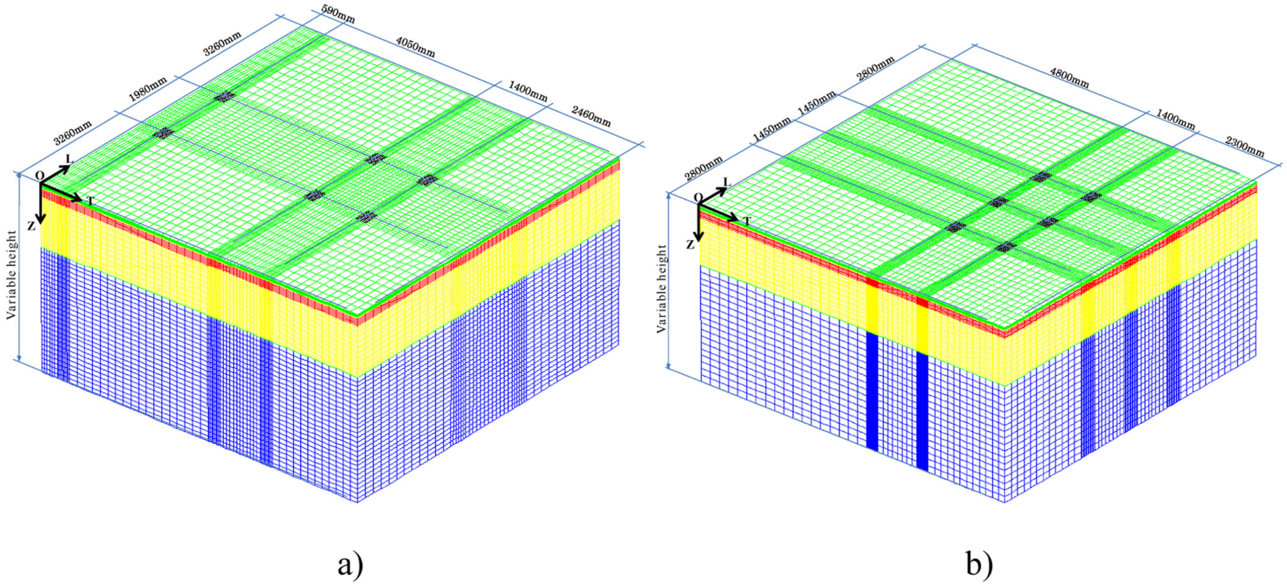

Figure 5: View of Cast3M 3D FEM of pavement on subgrade CBR = 3: (a) under landing gear of A340 and (b) under landing gear of a B777.

developed by Tornabene *et al.* [23] and Tornabene and Brischetto [24].

3.2 Boundary conditions of the 3D model under loading

The following boundary conditions are applied to the model used:

- Symmetry conditions are applied in the *LZ* plane (left side face). Thus, the displacements of the points of this plane are fixed along the axis *T*.
- The displacements of the points of the *LZ* plane (right side face) of the model are fixed along the *T* axis, because the mesh is limited transversely to a distance that is not large enough from the load.
- The displacements of the points of the two *TZ* planes (front face and rear face) of the model are fixed along the *L* axis, because we have limited our mesh longitudinally to a distance of approximately 1 m on either side of the load closer.
- The bottom of the subgrade layer (embedding plane of the substratum) is fixed in displacement, thus the displacements of the points of this plane are fixed along the axes *T*, *L*, and *Z*.

4 Numerical computational results

Figures 6–32 and Table 4 show the values of deflection and strain profiles in the different structures, we note the reduction in the maximum value of the deflections obtained with the different rigidities of the pavement subgrades, the type D structure is therefore more flexible (Table 4), and it is more deformable than the others. These maximum deflections are localized on the same point common to all the structures for each loading. We found high level of tensile strain at the bottom of base layer and very high vertical compressive strain at the top of UGM and subgrade, compared to "road" values [5,7,25–31].

At the base of GB, the signals of transverse and longitudinal strains are very clearly different. In the transverse direction, the base of GB is always in extension. The signal presents three or two peaks corresponding to the

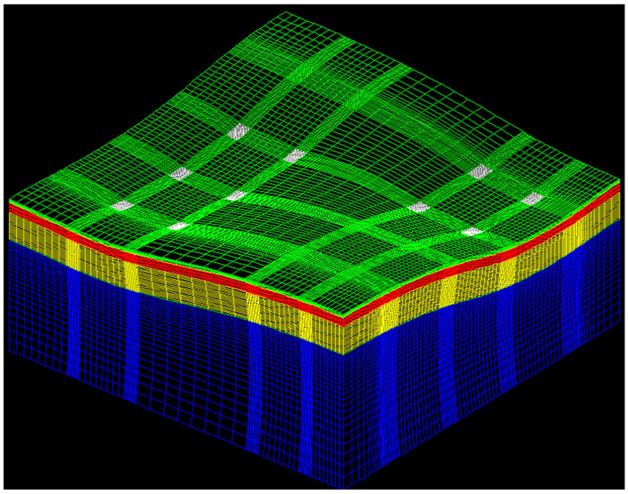

Figure 6: View of Cast3M 3D deformed mesh of pavement on the subgrade for CBR = 6.

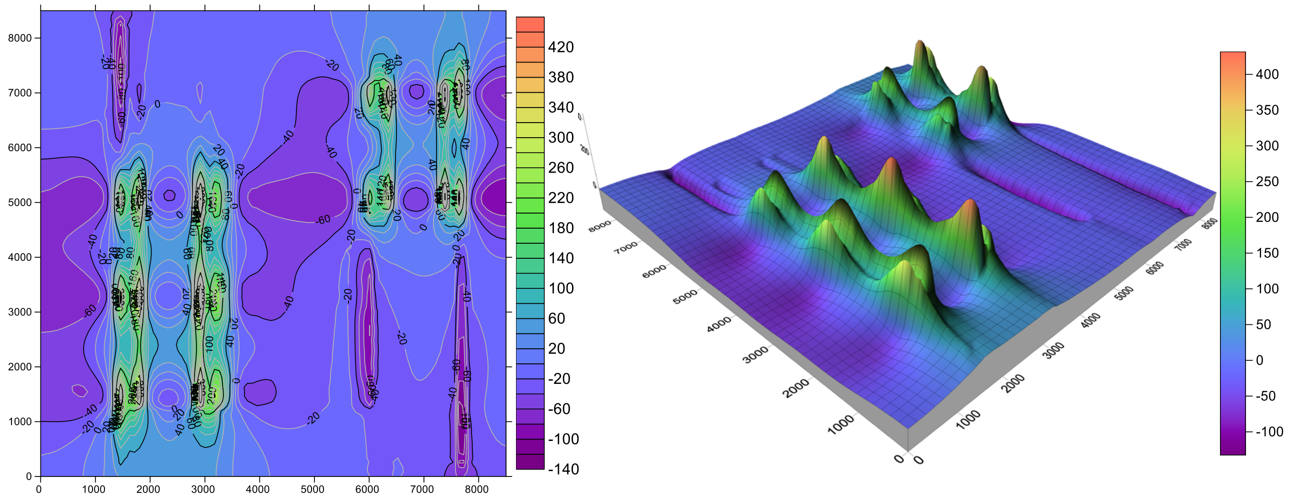

Figure 7: 3D and 2D views of transverse tensile strains (×10^{-6}) at the bottom of bituminous (GB) layer on the pavement for CBR = 3 in the subgrade.

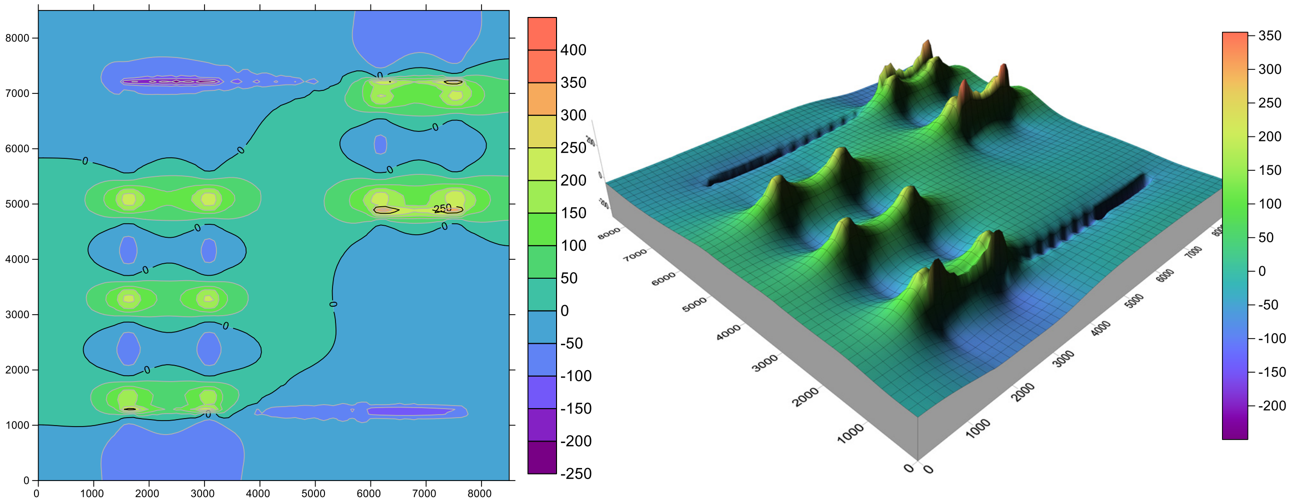

Figure 8: 3D and 2D views of longitudinal tensile strains (×10^{-6}) at the bottom of bituminous (GB) layer on the pavement for CBR = 3 in the subgrade.

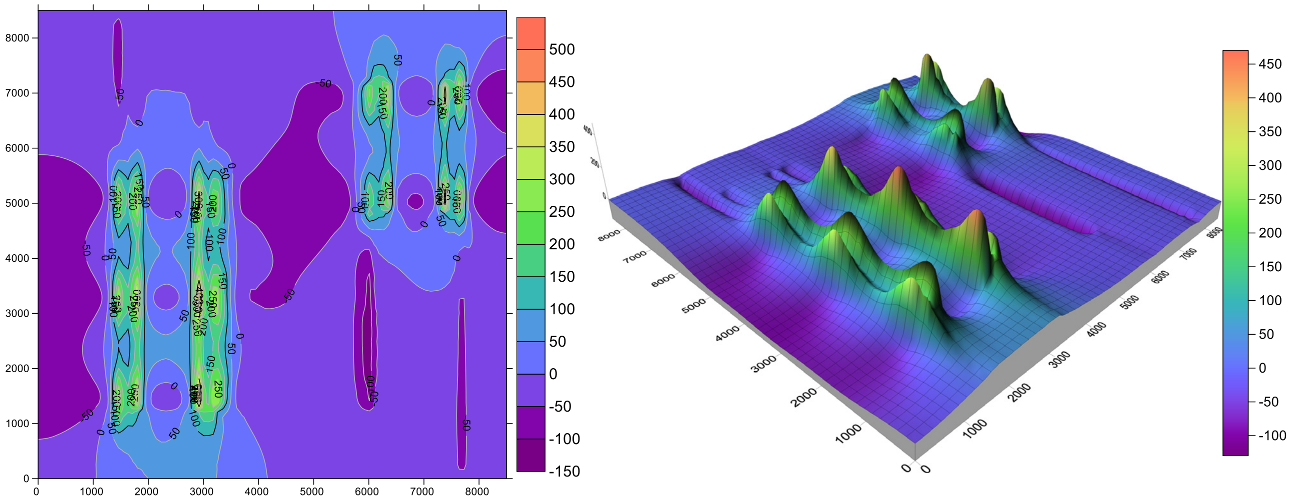

Figure 9: 3D and 2D views of transverse tensile strains (×10^{-6}) at the bottom of bituminous (GB) layer on the pavement for CBR = 6.

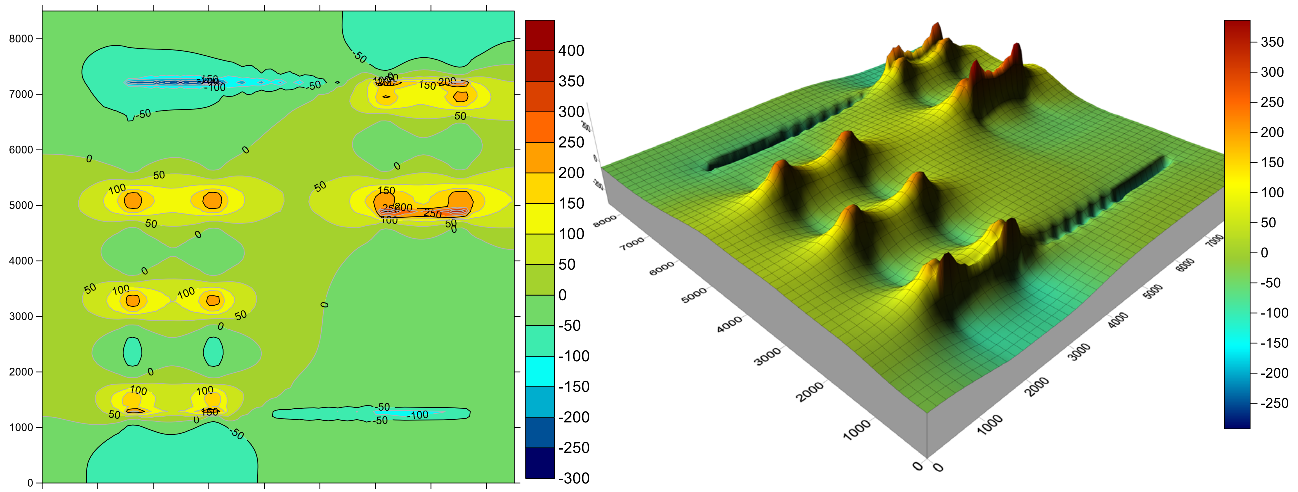

Figure 10: 3D and 2D views of longitudinal tensile strains (×10^{-6}) at the bottom of bituminous (GB) layer on the pavement for CBR = 6.

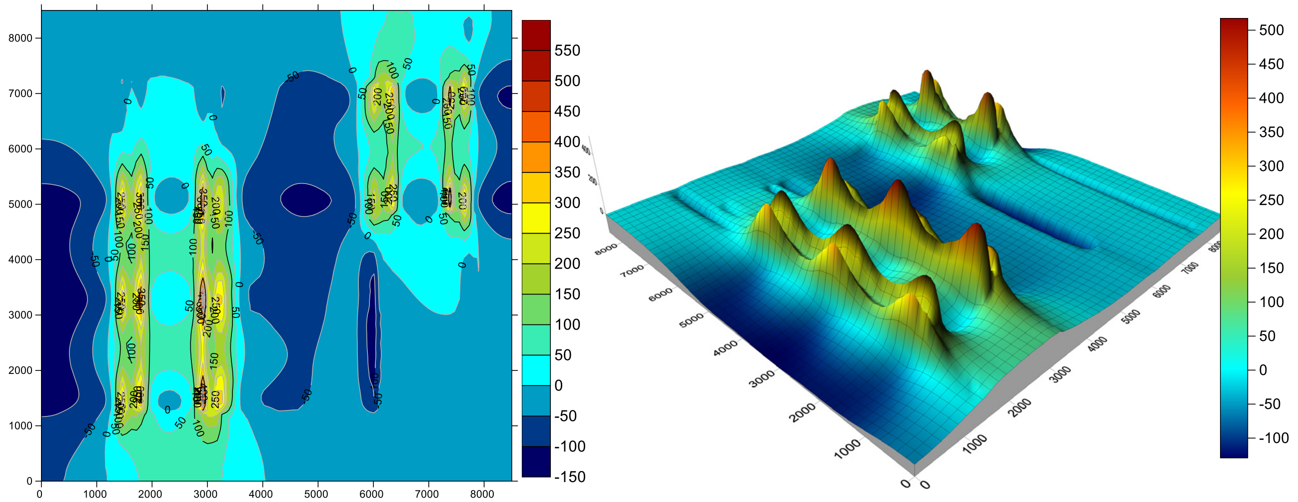

Figure 11: 3D and 2D views of transverse tensile strains (×10^{-6}) at the bottom of bituminous (GB) layer on the pavement for CBR = 10.

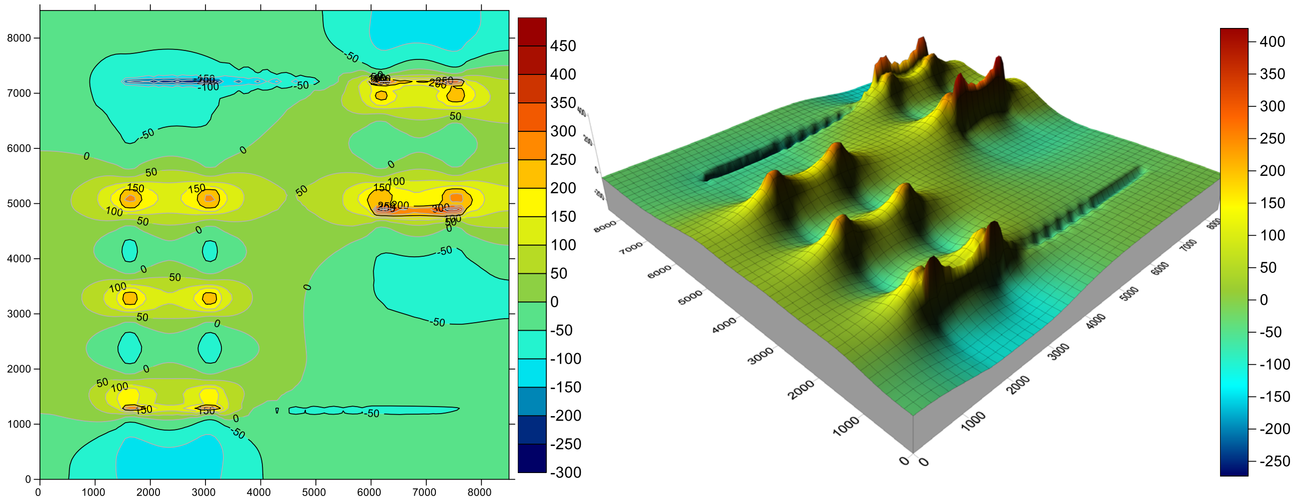

Figure 12: 3D and 2D views of longitudinal tensile strains (×10^{-6}) at the bottom of bituminous (GB) layer on the pavement for CBR = 10.

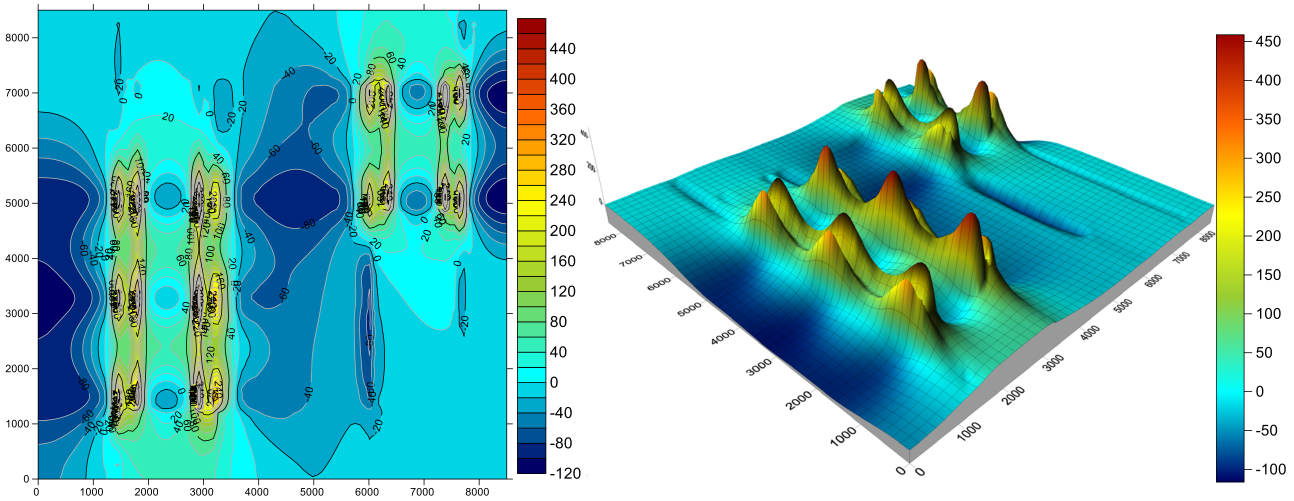

Figure 13: 3D and 2D views of transverse tensile strains (×10^{-6}) at the bottom of bituminous (GB) layer on the pavement for CBR = 15.

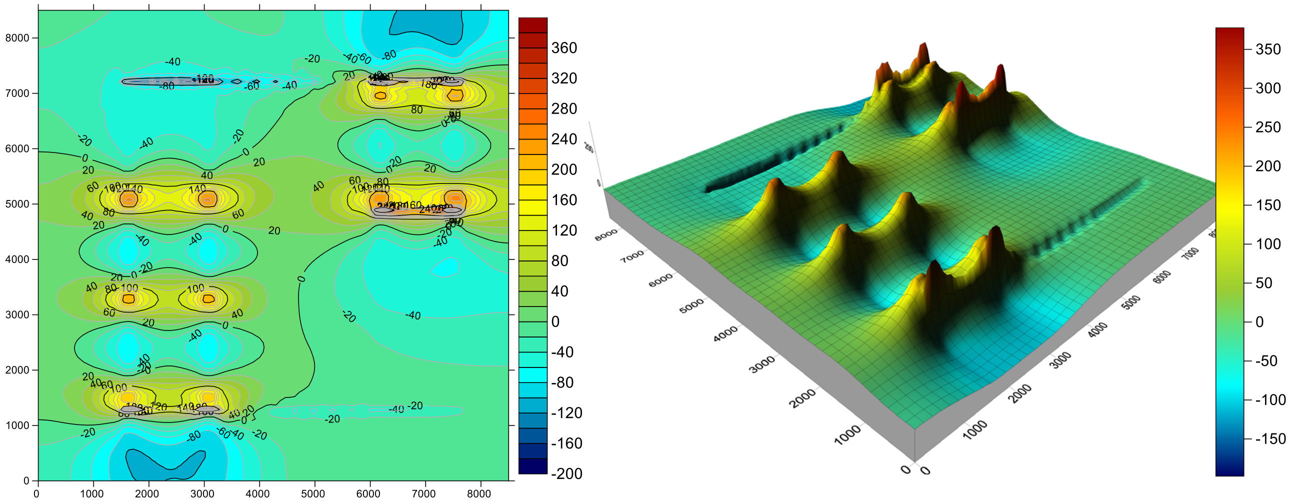

Figure 14: 3D and 2D views of longitudinal tensile strains (×10^{-6}) at the bottom of bituminous (GB) layer on the pavement for CBR = 15.

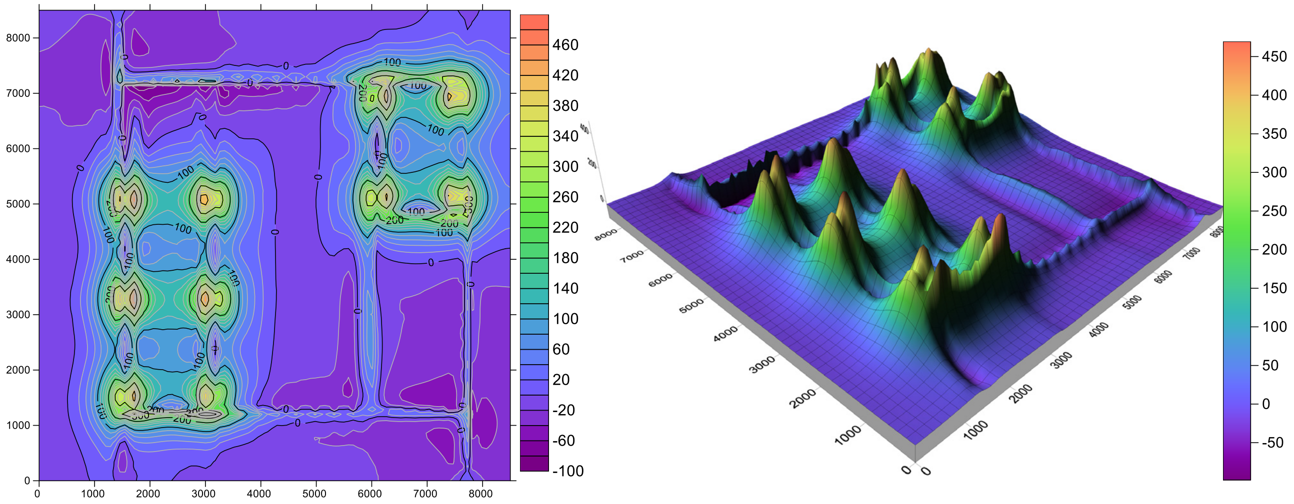

Figure 15: 3D and 2D views of vertical compressive strains (×10^{-6}) at the top of the UGM layer on the pavement for CBR = 3.

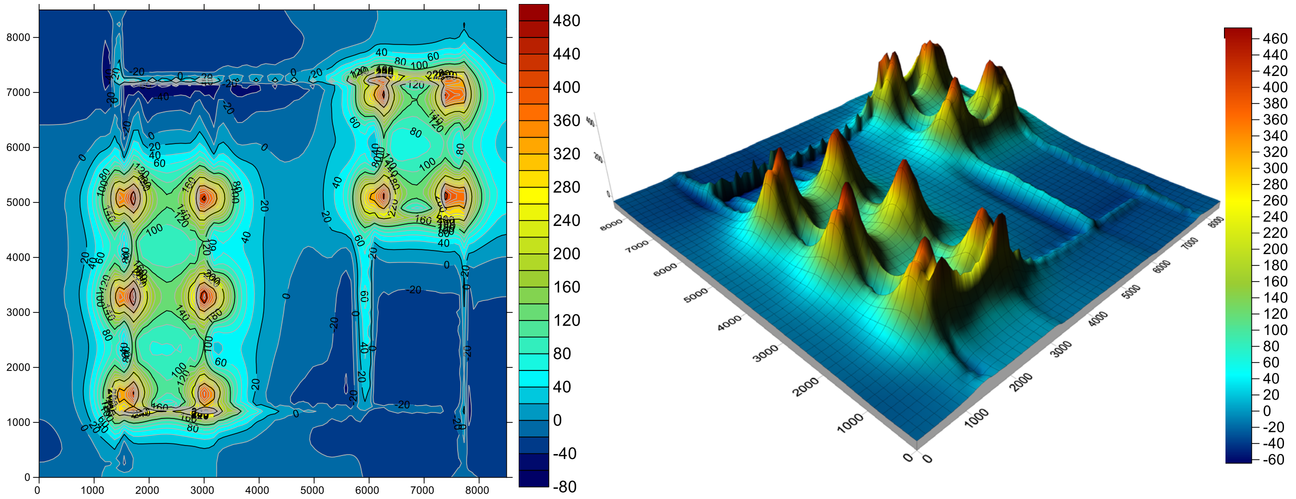

Figure 16: 3D and 2D views of vertical compressive strains (×10^{-6}) at the top of the UGM layer on the pavement for CBR = 6.

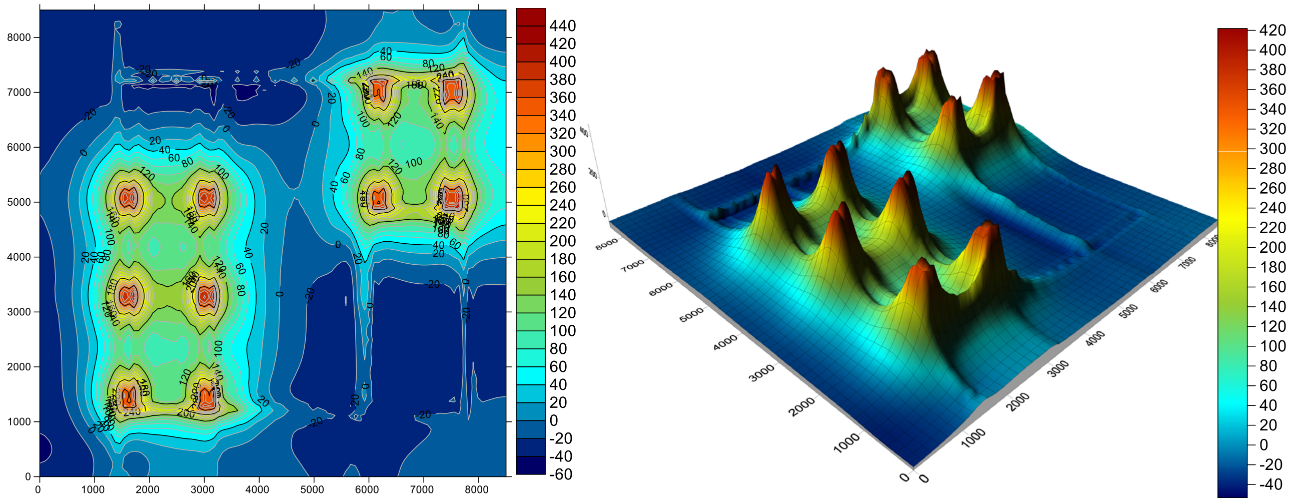

Figure 17: 3D and 2D views of vertical compressive strains (×10^{-6}) at the top of the UGM layer on the pavement for CBR = 10.

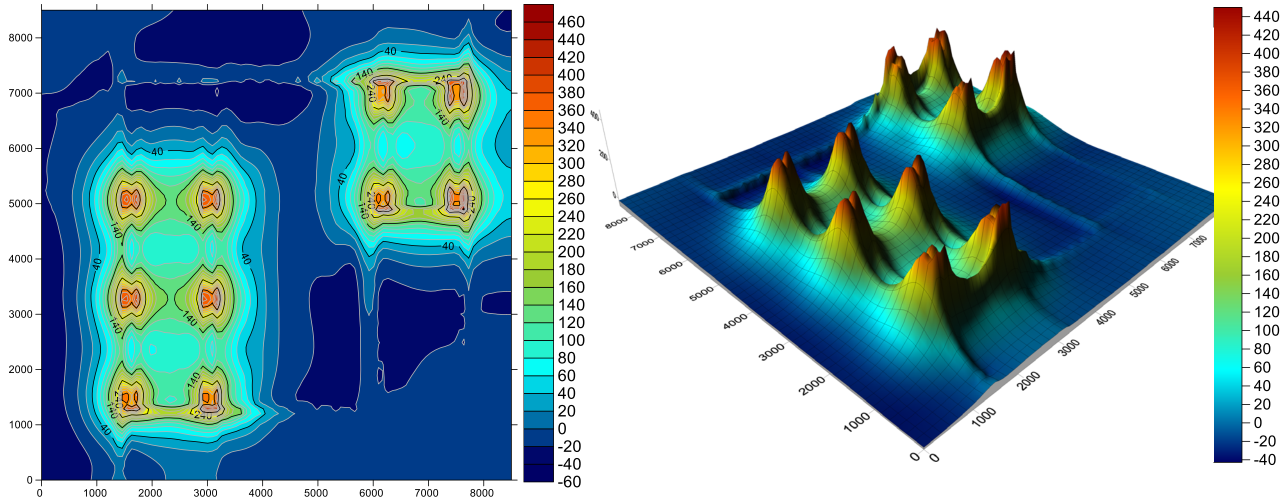

Figure 18: 3D and 2D views of vertical compressive strains (×10^{-6}) at the top of the UGM layer on the pavement for CBR = 15.

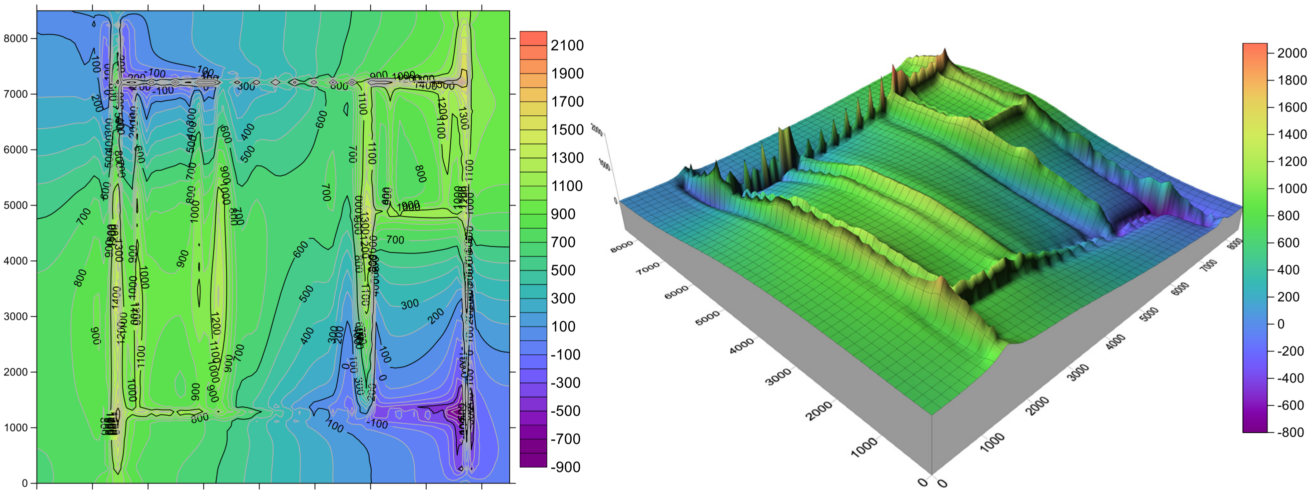

Figure 19: 3D and 2D views of vertical compressive strains (×10^{-6}) at the top of subgrade layer on the pavement for CBR = 3.

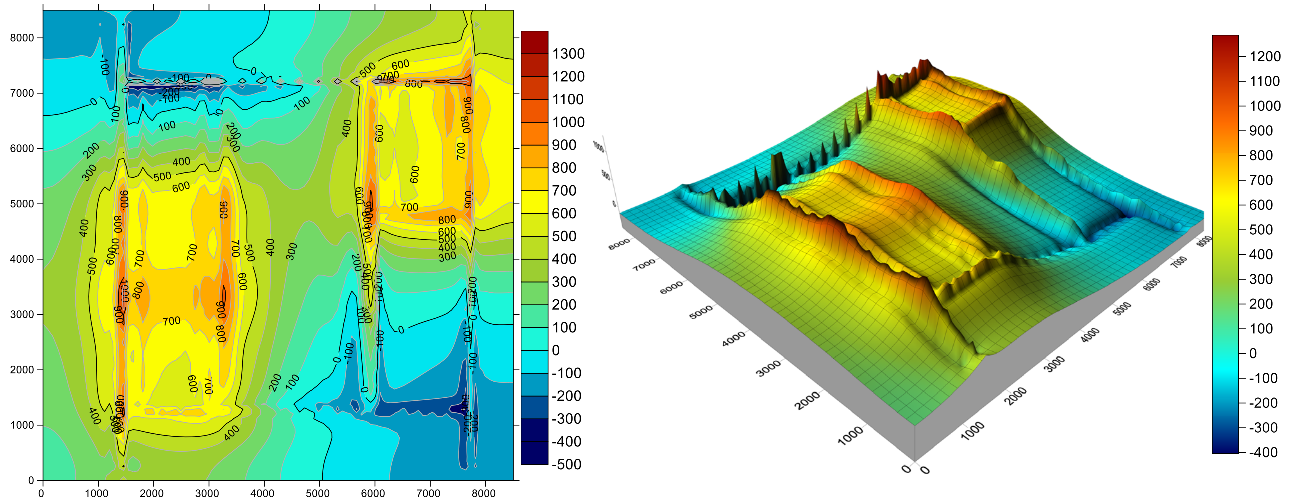

Figure 20: 3D and 2D views of vertical compressive strains (×10^{-6}) at the top of subgrade layer on the pavement for CBR = 6.

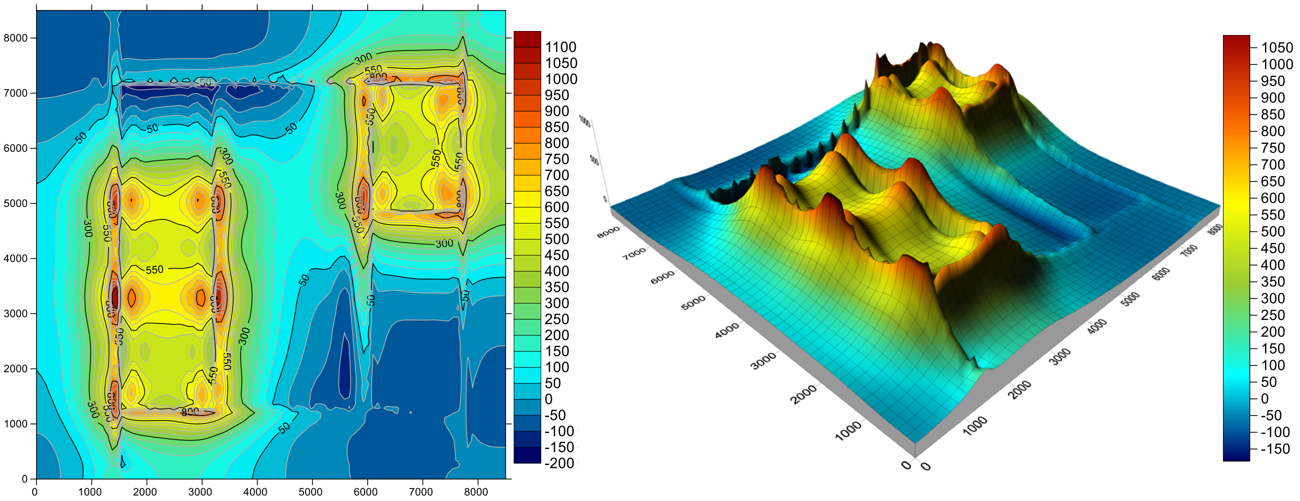

Figure 21: 3D and 2D views of vertical compressive strains (×10^{-6}) at the top of subgrade layer on the pavement for CBR = 10.

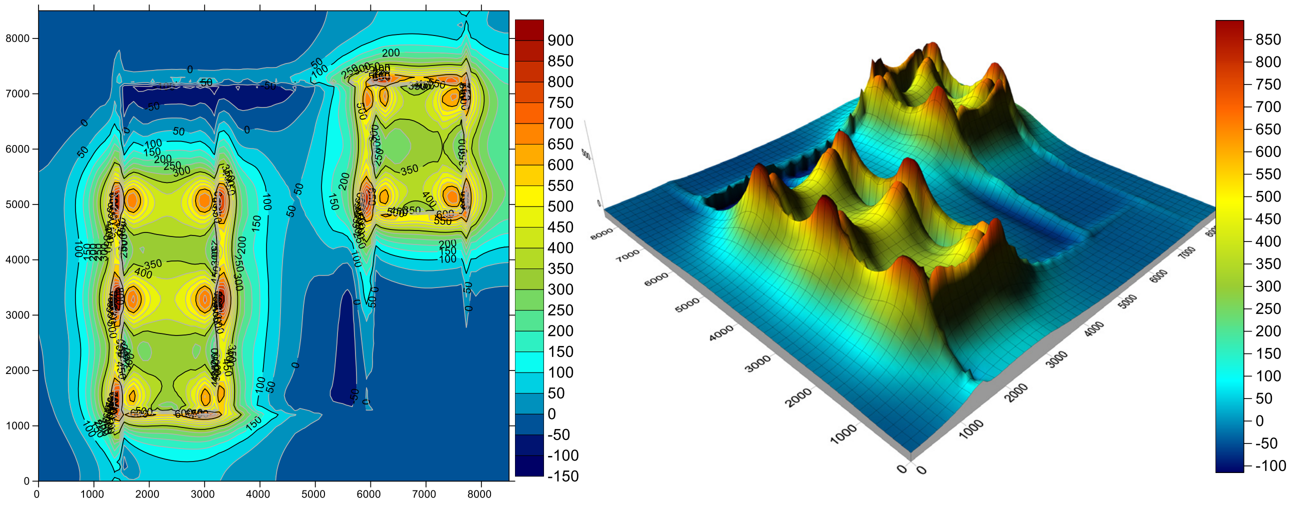

Figure 22: 3D and 2D views of vertical compressive strains (×10^{-6}) at the top of subgrade layer on the pavement for CBR = 15.

successive positions of the three or two axles composing the six- or four-wheels bogie. For three peaks in transverse direction, the inequality between the peak values is well marked. In this direction, the strain corresponding to the position of the second wheel is in most cases appreciably higher than those corresponding to the position of the first and third wheel. A perfectly elastic behaviour of materials would involve indeed a symmetry of the signal about the axis of the load (equality of the strains relative to the first and the third load). Such observations have been reported by Ambassa *et al.* [1,29,30], Priyanka and Tutumluer [2], Kerzrého *et al.* [5], Broutin [6], PEP [12], Homsi *et al.* [7], FCAA [14], Chatti and Salama [25] Chatti *et al.* [26], Salama and Chatti [27], Chabot *et al.* [28], and White [32] in their various experimental and numerical models.

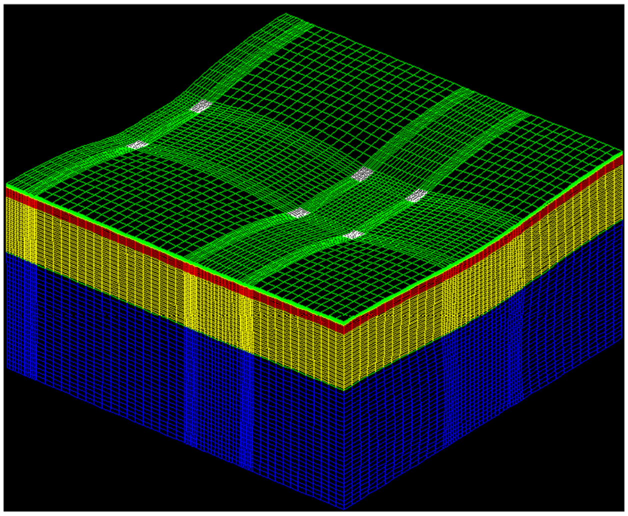

Figure 23: View of Cast3M 3D deformed mesh of pavement on the subgrade for CBR = 3.

In the longitudinal direction, the base of GB presents on the contrary successive shape of extension and compression: extension at the position of the wheels and compression between two wheels. The strain corresponding to the position of the second wheel is lower than the other two peaks (for six-wheels bogie). The tensile strains in the longitudinal direction corresponding to the position of the six-wheels bogie is lower than the strains in transverse direction in general. It is the opposite effect which is observed for the tensile strains generated for four-wheels bogie.

At the top of the UGM, the signal presents compression strains comprising two (four-wheels) or three separated peaks (six-wheels) per direction. In the case of the six-wheels bogie, the central peak has the greatest amplitude in general. At the top of the UGM and the top of the subgrade, the signals of the vertical strains have similar forms. They show a general compressive strain with the position of the load, with peaks under the wheels all the less marked as much than the layer of UGM is thick.

Figures 6–32 illustrate 3D and 2D views and shading of the strains at the base of the GB layer, at the top of the UGM and subgrade layers. The number of peaks in each 3D map indicates the position, types, and number of wheels bogie analysed on the pavements. These 3D shadings provide and improve all the necessary information at the bottom or at the top of each layer according to the design criteria considered.

4.1 Flexible pavements' response under landing gear of A380

The view of Cast3M 3D deformed mesh of pavement on the subgrade for CBR = 6 is shown in Figure 6.

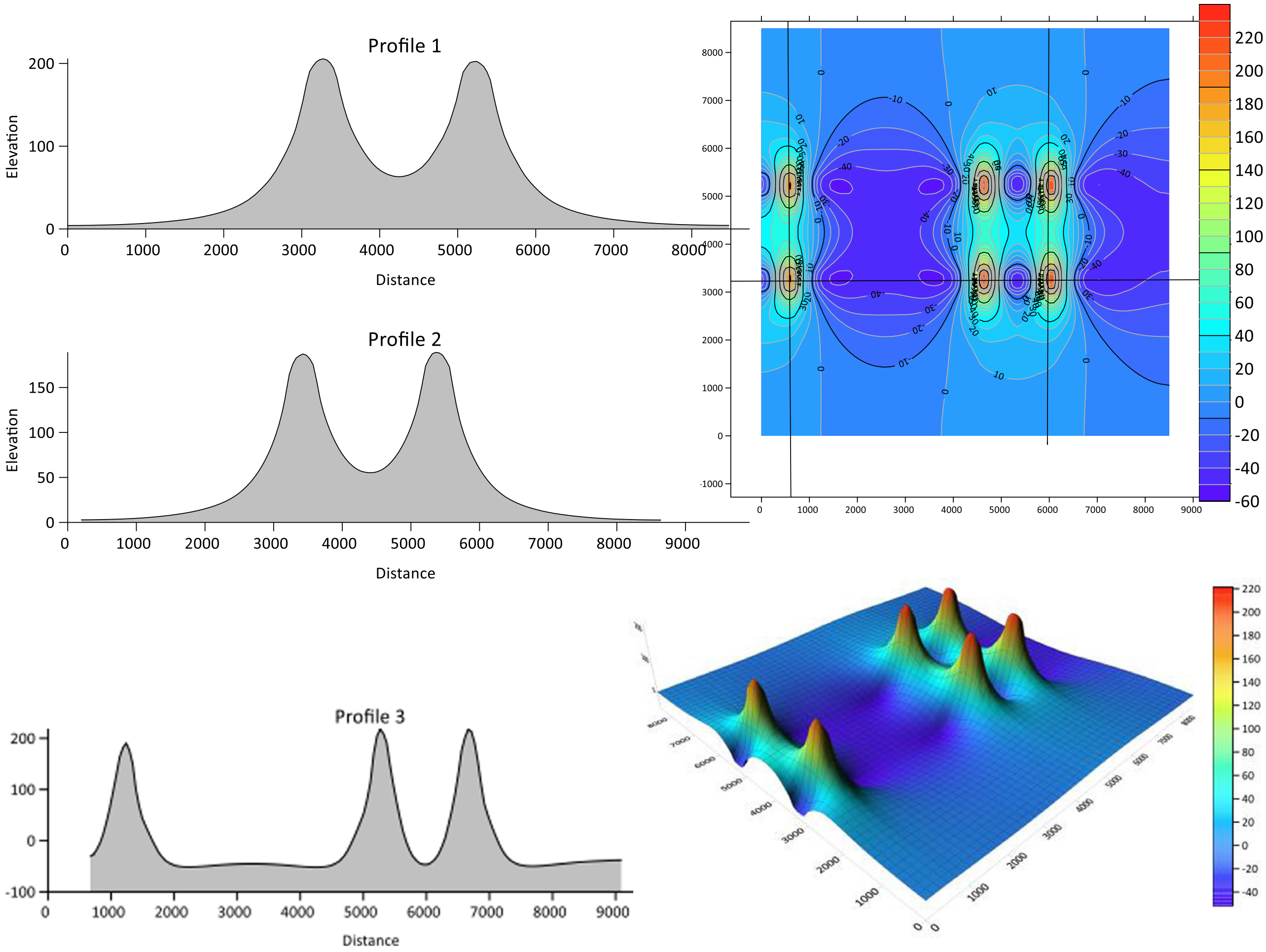

Figure 24: 3D and 2D views of transverse tensile strains (×10^{-6}) at the bottom of bituminous (GB) layer for CBR = 3.

4.1.1 Strains at the bottom of the GB3 layer (fatigue criterion)

The 3D and 2D views of transverse and longitudinal tensile strains (×10^{-6}) at the bottom of bituminous (GB) layer on the pavement for CBR = 3 in the subgrade are shown in Figures 7 and 8, respectively. The 3D and 2D views of transverse and longitudinal tensile strains (×10^{-6}) at the bottom of bituminous (GB) layer on the pavement for CBR = 6 are shown in Figures 9 and 10, respectively. While Figures 11 and 12 show the 3D and 2D views of transverse and longitudinal tensile strains (×10^{-6}) at the bottom of bituminous (GB) layer on the pavement for CBR = 10 and Figures 13 and 14 show the 3D and 2D views of transverse tensile strains (×10^{-6}) at the bottom of bituminous (GB) layer on the pavement for CBR = 15, respectively.

4.1.2 Strains at the top of the UGM layer (rutting criterion)

The 3D and 2D views of vertical compressive strains (×10^{-6}) at the top of the UGM layer on the pavement for CBR = 3, 6, 10, and 15 are shown in Figures 15–18, respectively.

4.1.3 Strains at the top of the subgrade layer (rutting criterion)

The 3D and 2D views of vertical compressive strains (×10^{-6}) at the top of subgrade layer on the pavement for CBR = 3, 6, 10, and 15 are shown in Figures 19–22, respectively.

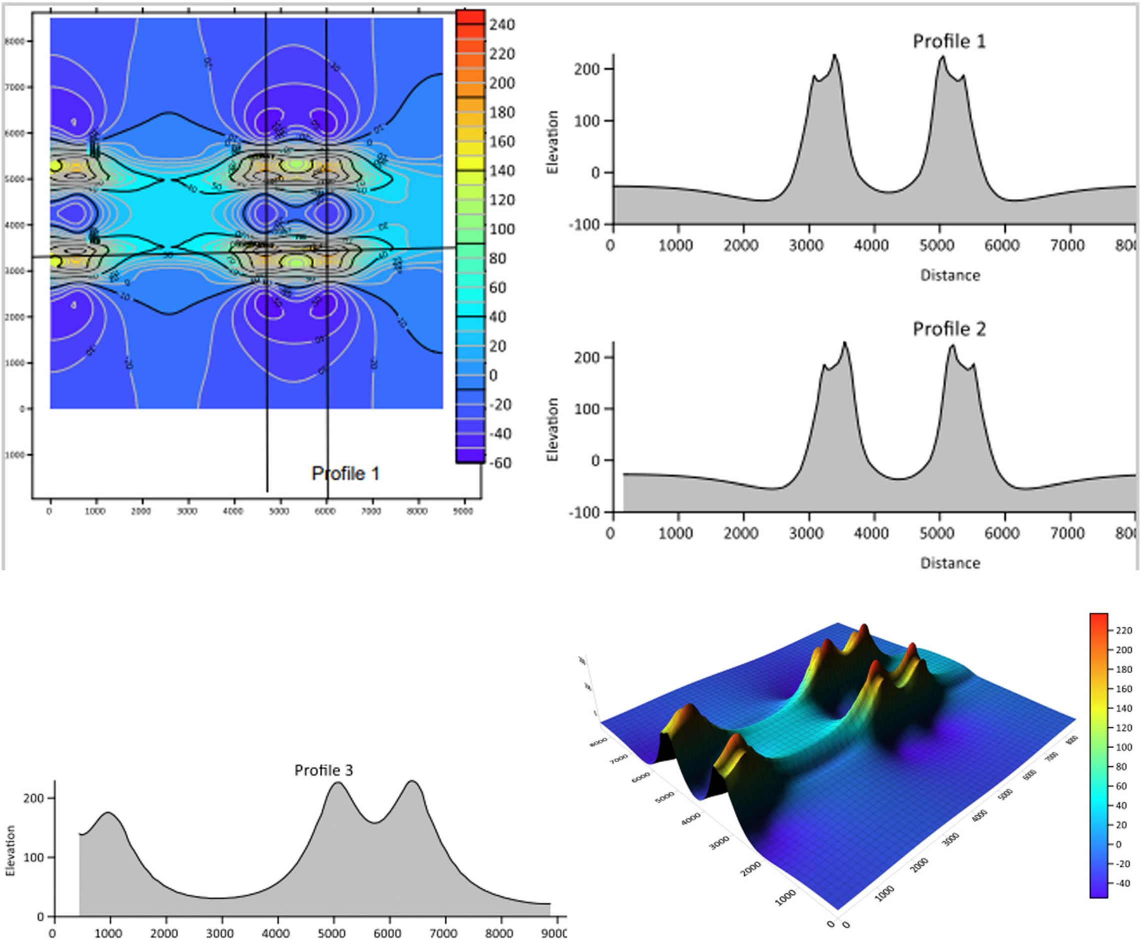

Figure 25: 3D and 2D views of longitudinal tensile strains (×10^{-6}) at the bottom of bituminous (GB) layer for CBR = 3.

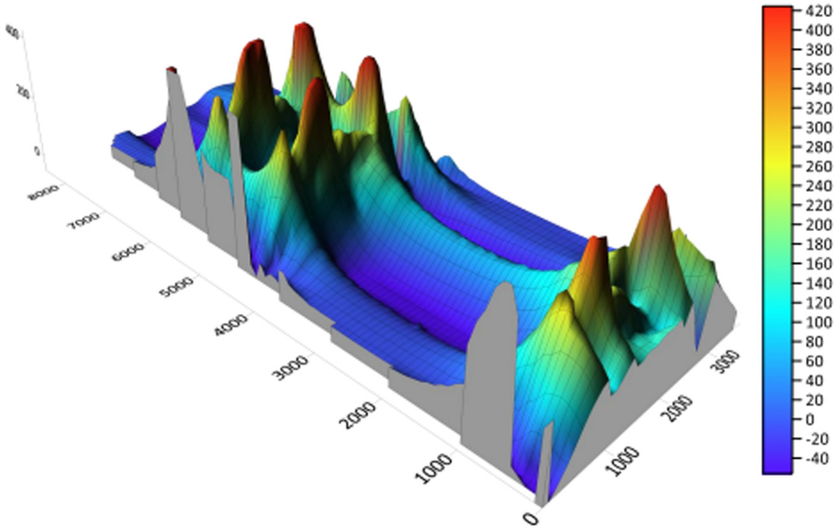

Figure 26: 3D view of vertical compressive strains (×10^{-6}) at the top of the UGM layer on the pavement for CBR = 3.

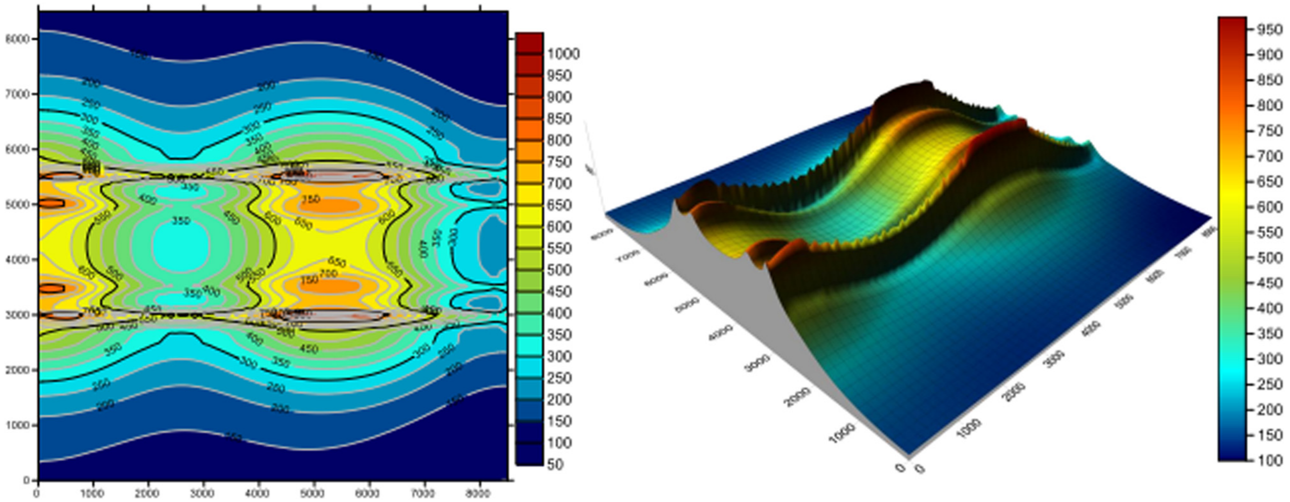

Figure 27: 3D and 2D views of vertical compressive strains ($\times 10^{-6}$) at the top of subgrade layer on the pavement for CBR = 3.

4.2 Flexible pavements' response under landing gear of A340-600

In Section 4.1, the mechanical responses in 2D and 3D planes of the four types of pavements with ICAO platforms were presented under loading of the A380 trucks at the bottom of the base course (transverse and longitudinal), at the top of the subbase layer, and at the top of the subgrade layer. In order to keep the article concise, only the response of a single type of pavement is presented in the following according to the other configurations of the landing gears. All results are summarized in Table 4.

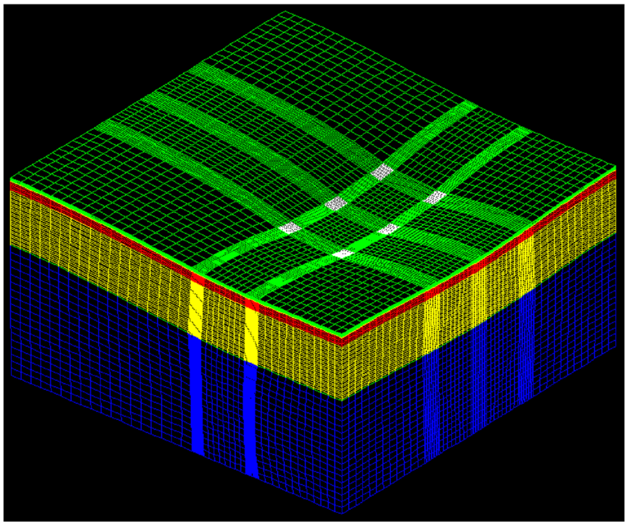

Figure 28: View of Cast3M 3-D deformed mesh of pavement on subgrade of the CBR = 3.

4.2.1 Strains at the base of GB3 layer (fatigue criterion)

The 3D and 2D views of transverse and longitudinal tensile strains ($\times 10^{-6}$) at the bottom of bituminous (GB) layer for CBR = 3 are shown in Figures 24 and 25, respectively.

4.2.2 Strains at the top of UGM layer (rutting criterion)

Figure 26 shows the 3D view of vertical compressive strains ($\times 10^{-6}$) at the top of the UGM layer on the pavement for CBR = 3.

4.2.3 Strains at the top of the subgrade layer (rutting criterion)

The 3D and 2D views of vertical compressive strains ($\times 10^{-6}$) at the top of subgrade layer on the pavement for CBR = 3 is shown in Figure 27.

4.3 Flexible pavements response under landing gear of B777-300ER

Figure 28 shows the View of Cast3M 3-D deformed mesh of pavement on the subgrade for CBR = 3.

4.3.1 Strains at the base of the GB3 layer (fatigue criterion)

The 3D and 2D views of transverse and longitudinal tensile strains ($\times 10^{-6}$) at the bottom of GB layer for CBR = 6 are shown in Figures 29 and 30, respectively.

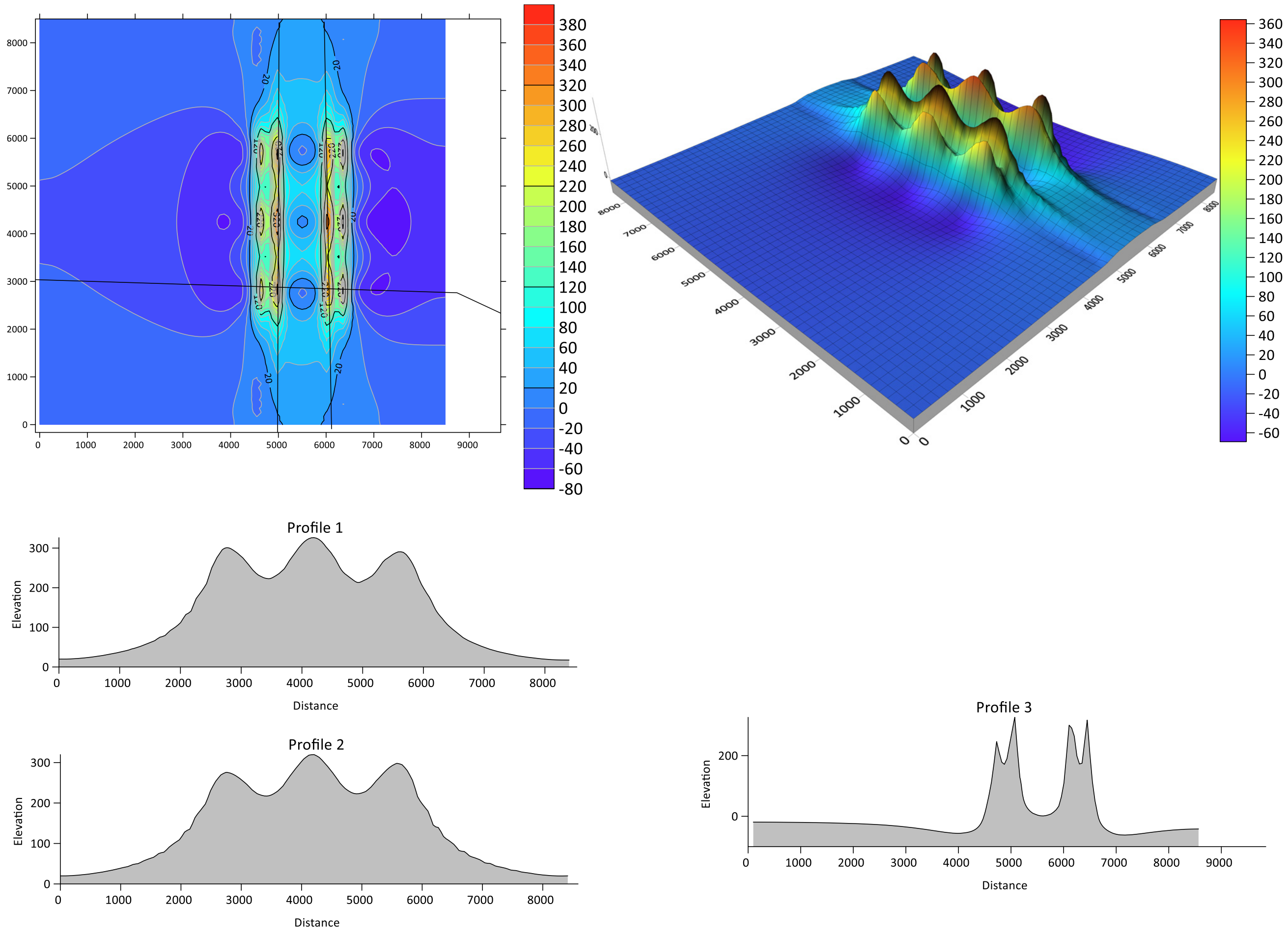

Figure 29: 3D and 2D views of transverse tensile strains (×10^{-6}) at the bottom of GB layer for CBR = 6.

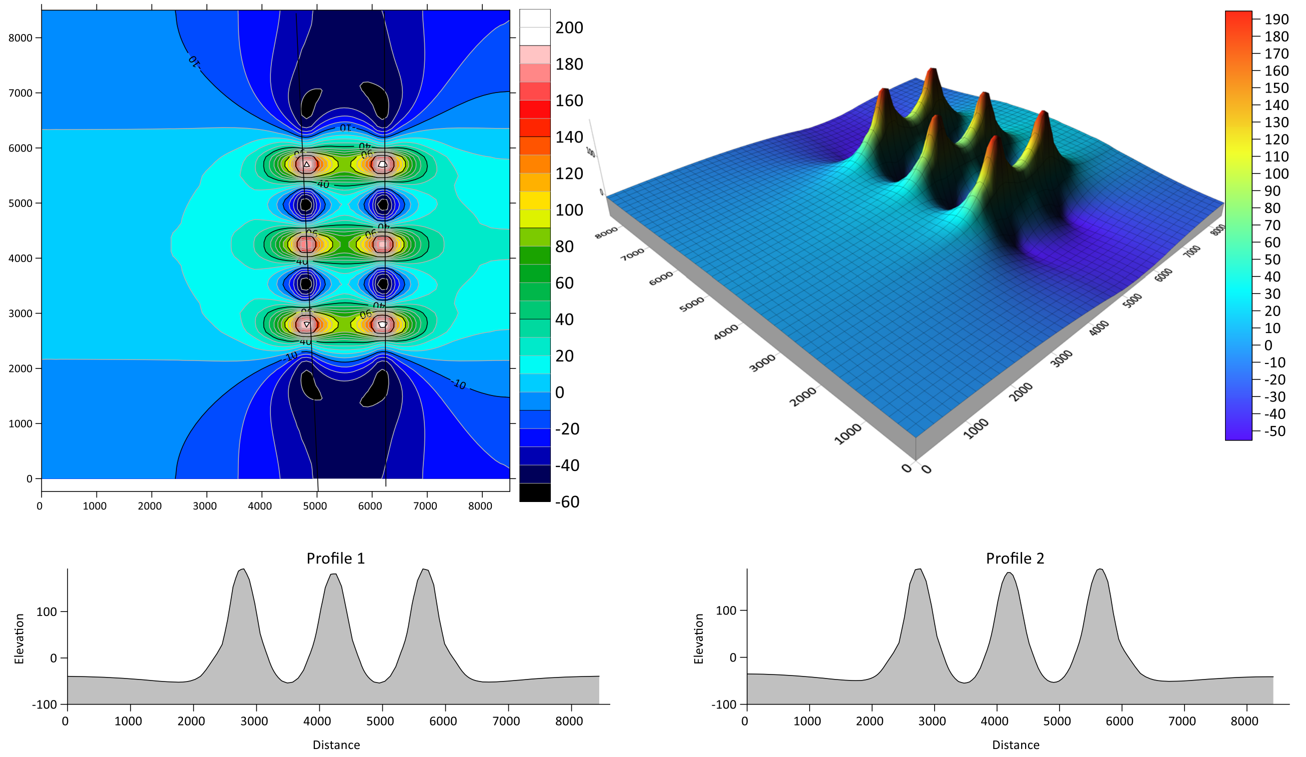

Figure 30: 3D and 2D views of longitudinal tensile strains (×10^{-6}) at the GB layer for CBR = 6.

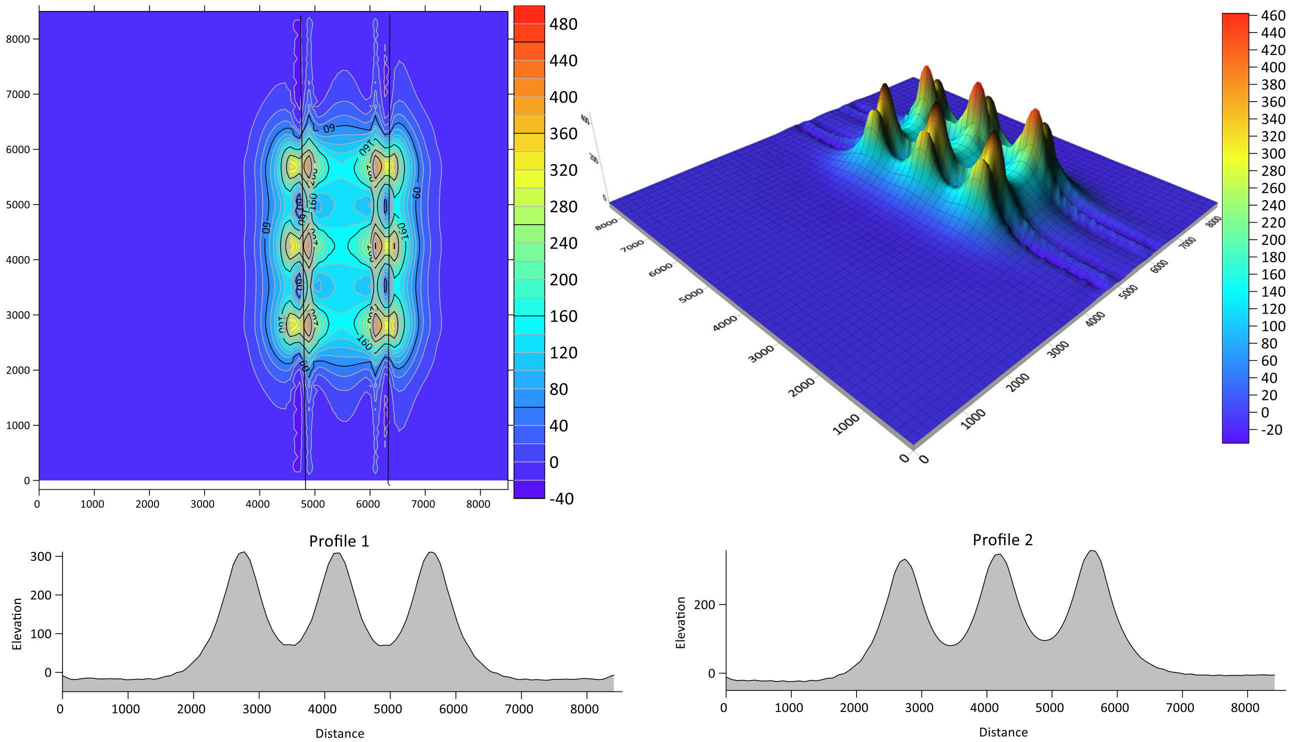

Figure 31: 3D and 2D views of vertical compressive strains ($\times10^{-6}$) at the top of the UGM layer on the pavement for CBR = 6.

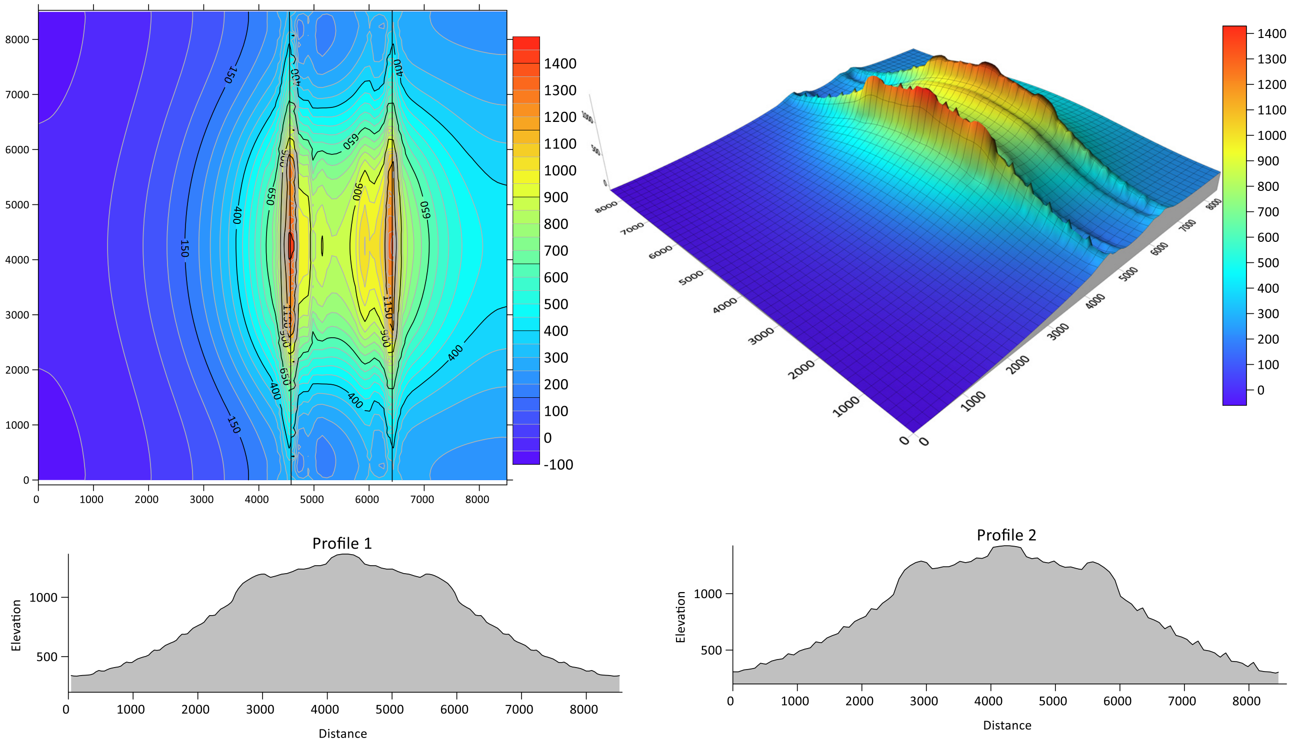

Figure 32: 3D and 2D views of vertical compressive strains ($\times10^{-6}$) at the top of subgrade layer on the pavement for CBR = 6.

Table 4: Summary of values of the deflections and the maximal strains in the pavement structures in transverse direction *T* and longitudinal direction *L*

Type of structure	Location in *T* (mm) and *L* (mm) of the maximal values of the model	Deflection at the surface of pavement (1/100 è mm)	Microstrains in the different layers of pavements			
			ε_{tT} at the base of the GB layer	ε_{tL} at the bottom of the GB layer	ε_Z at the top of UGM layer	ε_Z at the top of subgrade layer
			Critical pavement response to the bogies of Airbus 380			
Type A CBR = 15	Values	**196**	**459**	**378**	**−450**	**−893**
	(*T*, *L*)	(2,964, 5,217)	(2,919, 3,263)	(7,470, 4,894)	(7,641, 4,894)	(1,460, 3,263)
Type B CBR = 10	Values	**285**	**517**	**421**	**−422**	**−1,088**
	(*T*, *L*)	(2,964, 5,217)	(2,919, 3,263)	(7,470, 4,894)	(7,641, 4,894)	(1,460, 3,348)
Type C CBR = 6	Values	**365**	**470**	**386**	**−473**	**−1,287**
	(*T*, *L*)	(2,964, 5,256)	(2,919, 3,263)	(7,470, 4,894)	(1,717, 3,263)	(6,010, 7,212)
Type D CBR = 3	Values	**571**	**432**	**355**	**−469**	**−2,075**
	(*T*, *L*)	(2,964, 5,256)	(2,919, 3,263)	(6,268, 4,894)	(1,717, 3,263)	(6,010, 7,212)
			Critical pavement response to the bogies of Airbus 340-600			
Type A CBR = 15	Values	**153**	**246**	**250**	**−412**	**−724**
	(*T*, *L*)	(4,765, 5,007)	(6,010, 3,263/5,237)	(6,010, 3,434/5,066)	(6,010, 3,434/5,066)	(6,010, 3,005/5,495)
Type B CBR = 10	Values	**217**	**263**	**281**	**−427**	**−894**
	(*T*, *L*)	(5,160, 5,007)	(6,010, 3,263/5,237)	(6,010, 3,434/5,066)	(6,010, 3,434/5,066)	(4,722, 3,005/5,495)
Type C CBR = 6	Values	**248**	**240**	**261**	**−419**	**−867**
	(*T*, *L*)	(4,765, 5,007)	(6,010, 3,263/5,237)	(4,636, 3,434/5,066)	(6,010, 3,263/5,237)	(4,980, 3,005/5,495)
Type D CBR = 3	Values	**335**	**221**	**238**	**−423**	**−976**
	(*T*, *L*)	(4,765, 5,007)	(6,010, 3,263/5,237)	(4,636, 3,434/5,066)	(3,636, 3,348/5,152)	(5,152, 3,005/5,495)
			Critical pavement response to the bogies of B777-300ER			
Type A CBR = 15	Values	**200**	**382**	**212**	**−408**	**−1,042**
	(*T*, *L*)	(6,039, 4,250)	(4,980, 4,293)	(6,182, 2,833/5,667)	(6,354, 4,293)	(6,439, 4,293)
Type B CBR = 10	Values	**285**	**456**	**225**	**−435**	**−1,290**
	(*T*, *L*)	(6,039, 4,250)	(4,980, 4,293)	(6,182, 2,833/5,667)	(6,096, 4,293)	(6,439, 4,293)
Type C CBR = 6	Values	**333**	**364**	**195**	**−462**	**−1,486**
	(*T*, *L*)	(6,039, 4,250)	(4,980, 4,293)	(6,182, 2,833/5,667)	(6,096, 4,293)	(4,551, 4,293)
Type D CBR = 3	Values	**437**	**364**	**195**	**−462**	**−1,486**
	(*T*, *L*)	(6,039, 4,250)	(4,980, 4,293)	(6,182, 2,833/5,667)	(6,096, 4,293)	(4,551, 4,293)

4.3.2 Strains at the top of the UGM layer (rutting criterion)

Figure 31 shows the 3D and 2D views of vertical compressive strains ($\times 10^{-6}$) at the top of the UGM layer on the pavement for CBR = 6.

4.3.3 Strains at the top of the subgrade layer (rutting criterion)

The 3D and 2D views of vertical compressive strains ($\times 10^{-6}$) at the top of subgrade layer on the pavement for CBR = 6 is shown in Figure 32.

4.4 Flexible pavements response analysis

Table 4 displays the summarized values of the deflections, the maximal tensile strains in the longitudinal *L* and transverse *T* directions at the GB layer, the vertical compressive strains at the top of UGM layer and subgrade layer for four pavement structures under bogies' loads of A380, A340, and A380. The location of critical values on the model have been displayed in Table 4. For each bogie of the aircraft, the ratios of longitudinal *vs* transverse strains at the bottom of GB layer are displayed in Eqs. (2)–(4).

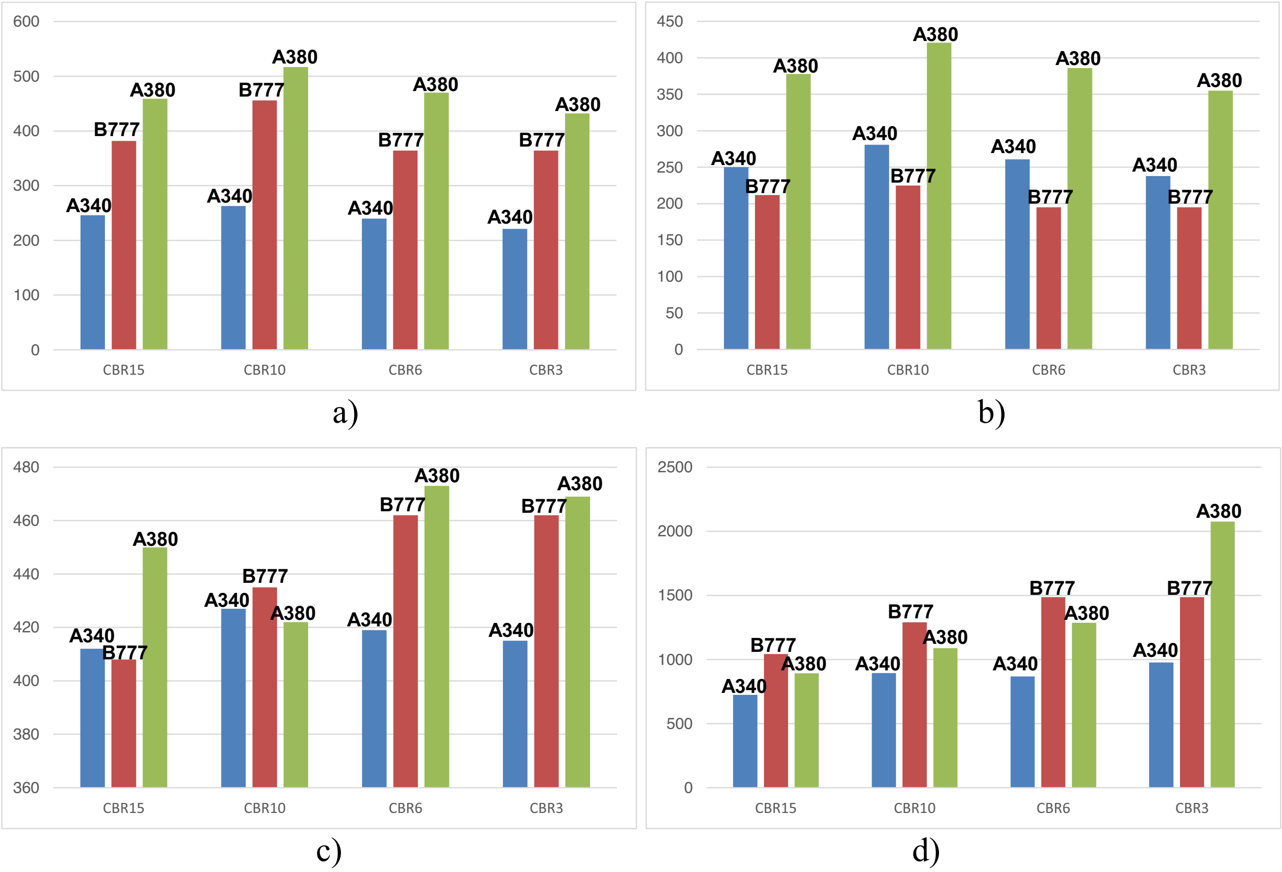

a) b) c) d)

Figure 33: Evolution of the level of microstrains according to the thickness of the subbase layer: (a) Transverse tensile microstrains at the GB layer; (b) longitudinal tensile microstrains at the GB layer; (c) compressive microstrains at the top of the subbase (UGM) layer; and (d) vertical compressive microstrains at the subgrade layer.

$$\left[\frac{\varepsilon_{t,L}}{\varepsilon_{t,T}}\right]_{A380,C7} = 0.82, \tag{2}$$

$$\left[\frac{\varepsilon_{t,L}}{\varepsilon_{t,T}}\right]_{A340-600} = 1.08, \tag{3}$$

$$\left[\frac{\varepsilon_{t,L}}{\varepsilon_{t,T}}\right]_{B777-300ER} = 0.54. \tag{4}$$

4.5 Influence of subbase thickness in different pavement structures

Figure 33 shows the evolution of the strains in the different structures under the heavy weight of various aircrafts. The pavement structures tested having the same characteristics in the bituminous layers and in the subgrade layer, but with a different subbase layer, show that the vertical compression deformations of the subgrade, respectively of the UGM, increase proportionally as a function of the thickness of the UGM in the different structures.

The more the thickness of the foundation layer (UGM) increases (because of the mechanical properties of the subgrade), the more the vertical strains increase in the subgrade and the UGM. On the other hand, the horizontal tensile strains (longitudinal and transverse) at the base of the bituminous gravel (GB) layer are higher when the thickness of the subbase layer decreases; therefore, the increase in these horizontal strains is inversely proportional to the thickness of the subbase layer.

4.6 Mechanical interpretation of the behaviour of the layers of materials under solicitation of the heavy loads

The mechanical behaviour of the layers of materials making up the pavement structure can be explained very well from

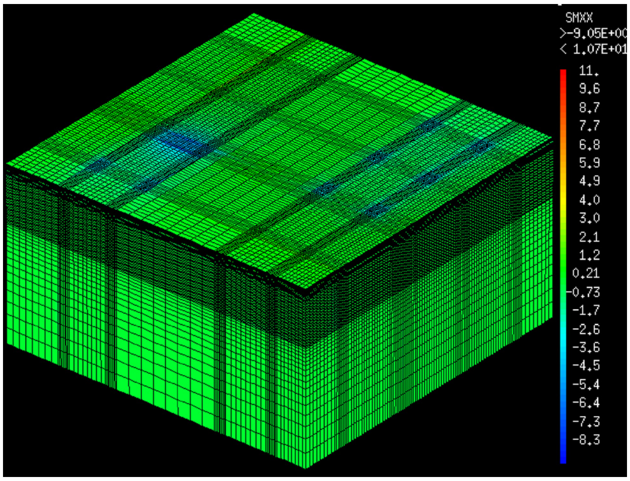

Figure 34: Shadings of transverse horizontal stresses (MPa) in the type B (CBR = 10) pavement structure under load from B777.

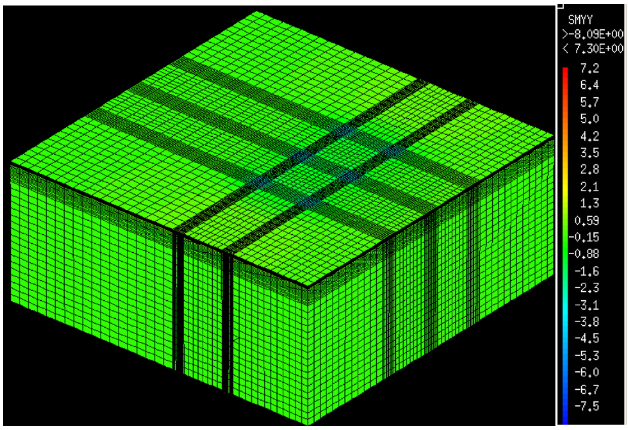

Figure 35: Shadings of the longitudinal horizontal stresses (MPa) in the type B (CBR = 10) pavement structure under load from B777.

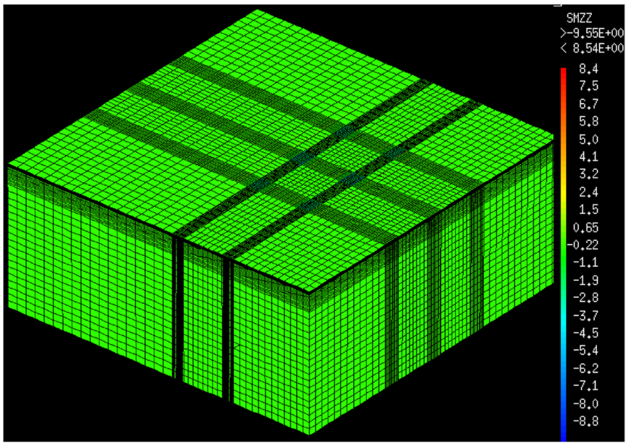

Figure 36: Shadings of vertical stresses (MPa) in the type B pavement structure under load from B777.

the evolution of the stress states in the structure under loading. Near the load surface, the materials are strongly compressed in all directions. The horizontal stresses are always greater than the vertical stresses, the bituminous materials are strongly stressed in traction horizontally than vertically (Figures 34–36), this even just in line with the load. The vertical stress is close to the tire/pavement contact pressure. In vertical strains, the materials are more stressed in compression than in tension. These stresses increase according to the loading and the configuration of the landing gear. The A380-800F is more restrictive for pavements. These observations make it possible to confirm that the requirements for the composition of bituminous mixes must be adapted according to the depth at which the materials are implemented.

At the top of the wearing course, where the forces are in compression, the quality of the granular composition of the bituminous mixture is crucial. On the other hand, the behaviour is different at the bituminous layers, where the materials constituting these layers are strongly stressed in traction for which the adhesion layer must be of superior quality to ensure perfect bonding at the interfaces.

5 Pavement damage calculation

The assessment of the damage to the pavement under aircraft bogie loading allows reliable predictions of the

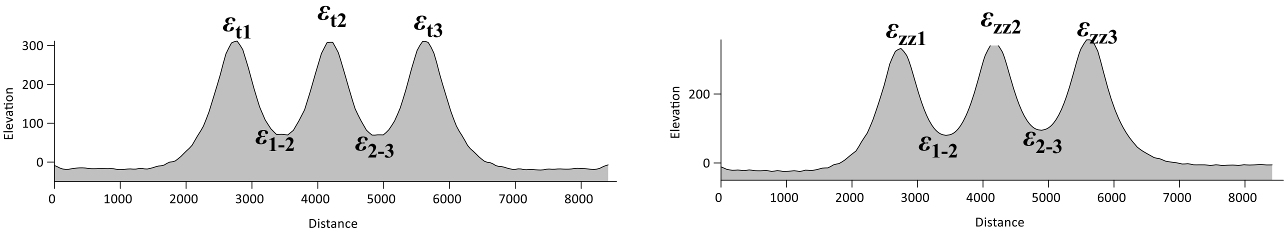

Figure 37: Method for extracting the peaks and troughs of strain to calculate the fatigue and rutting damage of airfield bituminous pavement.

Table 5: Summary fatigue parameters in the airfield pavement structures

Runway section: 100 km/h	Fatigue parameters	CBR = 3	CBR = 6	CBR = 10	CBR = 15
Thickness: (BB + GB) > 15 cm	S_h (cm)	2.5	2.5	2.5	2.5
GB material	S_N	0.3	0.3	0.3	0.3
	E (MPa) at (10°C, 10 Hz)	12,300	12,300	12,300	12,300
	E (MPa) at (15°C, 10 Hz)	9,300	9,300	9,300	9,300
	ε_6 at 10°C, 25 Hz (10^{-6} strains)	90	90	90	90
	c (m^{-1})	0.02	0.02	0.02	0.02
	b	−0.2	−0.2	−0.2	−0.2
	$k_{\theta f}$ (15°C, 10 Hz)	1.15	1.15	1.15	1.15
	δ	0.39	0.39	0.39	0.39
	u (risk: 2.5%)	−1.96	−1.96	−1.96	−1.96
	k_r	0.7	0.7	0.7	0.7
	k_c	2	2	2	2
	k_s	0.83	0.83	0.91	1.00
	K	1921.86	1921.66	2096.57	2306.23

service life of the pavement [2,14,32–34]. Top down and bottom up on airports flexible pavements cracking are evaluated in this section by new French Rational Design airports flexible pavements method (Figure 37), based on the concept of Rational Equivalent Simple Wheel Load (RseR) [14] (Eqs. (5) and (6)).

5.1 For fatigue criteria on the bituminous layers

$$\Delta D(x, z_k) = \frac{1}{K^\beta}[\varepsilon_{t_1}^\beta - \varepsilon_{u_{1-2}}^\beta + \varepsilon_{t_2}^\beta - \varepsilon_{u_{2-3}}^\beta + \cdots + \varepsilon_{t_n}^\beta], \quad (5)$$

where $\beta = -\frac{1}{b}$, $K = 10^{6/\beta} k_{\theta f} k_r k_s k_c \overline{\varepsilon}_6$, $\overline{\varepsilon}_6 = 90$ μstrains for GB materials,

$$k_{\theta f} = \sqrt{\frac{E(10\,^\circ\mathrm{C},\ 10\ \mathrm{Hz})}{E(\theta_{\mathrm{eq}}, f)}},\ k_r = 10^{-ub\delta}\ \ \delta = \sqrt{S_N^2 + \left(\frac{cS_h}{b}\right)^2},\ \text{and}$$

$k_c = 2$ for RseR > 25t

$$k_s = \begin{cases} \frac{1}{1.2} \geq E_{\mathrm{subgrade}} < 50\ \ \mathrm{MPa} \\ \frac{1}{1.1} \geq 50\ \ \mathrm{MPa} < E_{\mathrm{subgrade}} < 80\ \ \mathrm{MPa} \\ \frac{1}{1.065} \geq 80\ \ \mathrm{MPa} < E_{\mathrm{subgrade}} < 120\ \ \mathrm{MPa} \\ 1 \geq E_{\mathrm{subgrade}} \geq 120\ \ \mathrm{MPa}. \end{cases}$$

5.2 For rutting criteria at the top of the UGM and subgrade layers

$$\Delta D(x, z_k) = \frac{1}{K^\beta}[\varepsilon_{zz_1}^\beta - \varepsilon_{u_{1-2}}^\beta + \varepsilon_{zz_2}^\beta - \varepsilon_{u_{2-3}}^\beta + \cdots + \varepsilon_{zz_n}^\beta]. \quad (6)$$

$\Delta D(x, z_k) = \left(\frac{\varepsilon_{zz}}{K}\right)^\beta$, $K = 16{,}000$ and $\beta = 4.5$,

where ε_6 – (10°C, 25 Hz) tensile strain, at which fatigue failure of a sample of asphalt mix occurs upon 10^6 loading cycles (at 50% probability) under the following test conditions: bending of beam specimen at 10°C, at frequency of 25 Hz; ε_t – tensile strain, at which fatigue failure of a base the bituminous layer; ε_{zz} compressive strain, at which rutting failure of a top of the UGM and the subgrade layers; $b = -0.2$ – the slope of the fatigue line of asphalt mix; E(10°C) – the modulus of the bituminous material at 10°C; $E(\theta_{\mathrm{eq}})$ – the modulus of the bituminous material at equivalent design temperature; k_r – factor to account for variability of test results and calculation risk; S_N – The dispersion of the results of the fatigue tests on the asphalt concrete described by the standard deviation; S_h – the thickness of the layers made of bituminous binders is variable, with a dispersion that is expressed by the standard deviation; k_s – factor to account for errors in preparation of underneath asphalt layers; and k_c – factor to account for the type of asphalt mix (Table 5).

The analysis of the damage results of different structures while determining the value of the Rational Equivalent Simple Wheel Load (RseR) is very revealing:

- Regardless of the type of aircraft bogie considered in this study, the main mode of damage is the fatigue of the bituminous layers (Tables 6–9). On these bituminous layers, the elementary damage caused by bogie stress on the runway is much greater than the damage obtained on the layers of unbound materials (UGM and the subgrade), which is linked to rutting.
- This investigation demonstrates that the trend, which aims to reduce the load of the four- and six-wheels bogies

Table 6: Damage calculation results in the airfield pavement structures for bogie of A380

Aircraft type: A380 – Six-wheels bogies					
	Peak 1	**432**	**470**	**517**	**459**
Criterion 1	Trough 1	175	200	210	175
Transversal strains (µstrains) at the base of GB3 (p1)	Peak 2	**432**	**470**	**517**	**459**
	Trough 2	175	200	210	175
	Peak 3	**432**	**470**	**517**	**459**
	Δ*D*	**1.71×10^{-3}**	**2.60×10^{-3}**	**2.72×10^{-3}**	**9.32×10^{-4}**
	Peak 1	**355**	**386**	**421**	**378**
Criterion 1	Trough 1	−50	−100	−90	−100
Longitudinal strains (µstrains) at the base of GB3 (p1)	Peak 2	**355**	**386**	**421**	**378**
	Trough 2	−50	−100	−90	−100
	Peak 3	**355**	**386**	**421**	**378**
	Δ*D*	**6.45×10^{-4}**	**9.81×10^{-4}**	**9.80×10^{-4}**	**3.55×10^{-4}**
	$\Delta D_{\text{Bottom of GB3 layer}}$	**1.71×10^{-3}**	**2.60×10^{-3}**	**2.72×10^{-3}**	**9.32×10^{-4}**
	RseR (t)	**65.99**	**66**	**67.20**	**62.27**
	$\varepsilon_{t,\text{RseR}}$ (µstrains)	**537.37**	**584.40**	**643.09**	**571.17**
Criterion 2	**K**	**16,000**	**16,000**	**16,000**	**16,000**
Vertical strains at the top of UGM	Peak 1	**469**	**473**	**422**	**450**
	Trough 1	100	90	110	120
	Peak 2	**469**	**473**	**422**	**450**
	Trough 2	100	90	110	120
	Peak 3	**469**	**473**	**422**	**450**
	Δ*D*	**3.79×10^{-7}**	**3.94×10^{-7}**	**2.35×10^{-7}**	**3.14×10^{-7}**
Criterion 2	**K**	**16,000**	**16,000**	**16,000**	**16,000**
Vertical strains at the top of the subgrade	Peak 1	**1,950**	**1,200**	**1,065**	**880**
	Trough 1	1,900	1,100	800	550
	Peak 2	**2,075**	**1,287**	**1,088**	**893**
	Trough 2	1,900	1,100	800	550
	Peak 3	**1,950**	**1,200**	**1,065**	**880**
	Δ*D*	**1.19×10^{-4}**	**1.75×10^{-5}**	**1.29×10^{-5}**	**6.07×10^{-6}**

of an undercarriage to an Equivalent Single Wheel in order to determine the thickness of the pavement according to the rutting criterion of the material layers, is not always suitable; especially for the stresses of large aircraft whose preponderant effect on bituminous pavements is rather the fatigue damage of the bituminous layers.

- From the pavement structure point of view according to the ACN/PCN method, the four categories of pavements depending on the value of CBR of the subgrade are theoretically equivalent, as they are compensated by a subbase layer of UGM whose thickness increases according to low CBR values to compensate for the low lift of the subgrade. Analysis of the results of 3D numerical modelling and damage calculations through strains shows that the load transfer mechanism is very different from one pavement to another and is a function of the position and composition of the bogies. Structure A (CBR of platform = 15) presents a better mechanical behaviour (damage by fatigue of GB) than others whatever the configuration of the loading. Then, the other structures (B, C, and D) present different behaviours according to the requests, thus one can observe that the structure D has a better behaviour than B and C when it is requested for the four-wheels bogies of A340 and the four- and six-wheels bogies of A380, but much less better when called upon for the six-wheels bogies of B777. In general, structure B behaves less well than the others, except when it is stressed by the four-wheels bogie of A340, whose behaviour is better than structure C. In view of this study, for new construction of airport pavements on low bearing subgrade sites, it is rather advantageous to improve the bearing capacity of these soils to bring them to a minimum CBR of 15 than to compensate for the lack of bearing capacity on the subgrade layer.
- From the fatigue point of view of the bituminous layers, there are two types of cracks which appear when each aircraft passes; the predominance of transverse cracking is noted when the pavement is stressed by A340-600; on

Table 7: Damage calculation results in the airfield pavement structures for bogie of B777

Aircraft type: B777-300 ER – Six-wheels bogies					
	Peak 1	**230**	**355**	**270**	**375**
Criterion 1	Trough 1	220	250	210	190
Transversal strains (µstrains) at the base of GB3 (p1)	Peak 2	**364**	**364**	**320**	**382**
	Trough 2	220	250	210	190
	Peak 3	**340**	**355**	**320**	**375**
	ΔD	**4.02×10^{-4}**	**5.99×10^{-4}**	**1.81×10^{-4}**	**3.44×10^{-4}**
	Peak 1	**364**	**320**	**370**	**375**
	Trough 1	220	230	300	190
Transversal strains (µstrains) at the base of GB3 (p2)	Peak 2	**364**	**364**	**456**	**382**
	Trough 2	220	230	300	190
	Peak 3	**364**	**360**	**370**	**375**
	ΔD	**6.92×10^{-4}**	**5.59×10^{-4}**	**7.09×10^{-4}**	**3.44×10^{-4}**
Criterion 1	Peak 1	**195**	**195**	**225**	**212**
	Trough 1	−50	−56	−35	−65
Longitudinal strains (µstrains) at the base of GB3 (p1)	Peak 2	**187**	**187**	**220**	**200**
	Trough 2	−50	−56	−35	−65
	Peak 3	**195**	**195**	**225**	**212**
	ΔD	**3.03×10^{-5}**	**3.03×10^{-5}**	**4.12×10^{-5}**	**1.81×10^{-5}**
	$\Delta D_{\text{Bottom of GB3 layer}}$	**6.92×10^{-4}**	**5.99×10^{-4}**	**7.09×10^{-4}**	**3.44×10^{-4}**
	RseR (t)	**55.07**	**49.23**	**51.37**	**51.00**
	$\varepsilon_{t,\text{RseR}}$ (µstrains)	**448.46**	**435.77**	**491.65**	**468.08**
Criterion 2	**K**	**16,000**	**16,000**	**16,000**	**16,000**
Vertical strains at the top of UGM	Peak 1	**462**	**462**	**430**	**400**
	Trough 1	100	80	180	170
	Peak 2	**462**	**462**	**435**	**408**
	Trough 2	100	80	180	170
	Peak 3	**462**	**462**	**430**	**400**
	ΔD	**3.54×10^{-7}**	**3.54×10^{-7}**	**2.58×10^{-7}**	**1.88×10^{-7}**
Criterion 2	**K**	**16,000**	**16,000**	**16,000**	**16,000**
Vertical strains at the top of the subgrade	Peak 1	**1,350**	**1,350**	**1,100**	**968**
	Trough 1	1,300	1,300	1,000	722
	Peak 2	**1,486**	**1,486**	**1,290**	**1,042**
	Trough 2	1,300	1,300	1,000	722
	Peak 3	**1,350**	**1,350**	**1,100**	**968**
	ΔD	**2.73×10^{-5}**	**2.73×10^{-5}**	**1.61×10^{-5}**	**9.42×10^{-6}**

the other hand, aircrafts of A380-800F and B777-300ER type create more longitudinal cracking. By observing the critical zone at the passage of each aircraft, on the various pavement structures, it is noted that the critical damage is located to the right of the four-wheels bogies for aircraft of A340-600 type. Also, this critical damage is located in line with the six-wheels bogies for aircraft of A380-800F and B777-300ER types.

This investigation on airfield pavements confirms that six-wheels bogies for aircraft or tridem axles of heavy weights on road pavement mainly create longitudinal cracking due to the maximum transverse strains, while four-wheels bogie for aircraft or tandem axles mainly create transverse cracking due to the maximum longitudinal strains such as in road pavements.

In the case of heterogeneous traffic in aircraft, Miner's [35] additivity law is applied to have an equivalent damage. If a reference aircraft A340 is assumed, the total damage of equivalent axles corresponding to the traffic mix is calculated as follows:

$$\frac{n_0}{N_0} + \frac{n_1}{N_1} + \frac{n_2}{N_2} = 1, \tag{7}$$

$$D = \left[n_0 \Delta D_{\text{A340}} + n_1 \left(\frac{\Delta D_{\text{A340}}}{\Delta D_{\text{B777}}} \right) + n_2 \left(\frac{\Delta D_{\text{A340}}}{\Delta D_{\text{A380}}} \right) \right], \tag{8}$$

where ΔD is the damage for one passage of bogie to the aircraft considered; n_0, n_1, and n_2 are, respectively, the number of axles load passing for a bogie of A340, B77, and A380 for the design criterion (fatigue or rutting) of airfield flexible pavement. N_0, N_1, and N_2 are, respectively,

Table 8: Damage calculation results in the airfield pavement structures for bogie of A340

Aircraft type: A340-600 – four-wheels bogies					
	Peak 1	**221**	**240**	**263**	**246**
Criterion 1	Trough 1	60	80	100	105
Transversal strains (μstrains) at the base of GB3 (p1)	Peak 2	**221**	**240**	**263**	**246**
	ΔD	$\mathbf{4.02 \times 10^{-5}}$	$\mathbf{6.06 \times 10^{-5}}$	$\mathbf{6.19 \times 10^{-5}}$	$\mathbf{2.74 \times 10^{-5}}$
	Peak 1	**238**	**261**	**281**	**250**
Criterion 1	Trough 1	−40	−35	−20	−35
Longitudinal strains (μstrains) at the base of GB3 (p1)	Peak 2	**238**	**261**	**281**	**250**
	ΔD	$\mathbf{5.83 \times 10^{-5}}$	$\mathbf{9.24 \times 10^{-5}}$	$\mathbf{8.65 \times 10^{-5}}$	$\mathbf{2.99 \times 10^{-5}}$
	$\Delta D_{\text{Bottom of GB3 layer}}$	$\mathbf{5.83 \times 10^{-5}}$	$\mathbf{9.24 \times 10^{-5}}$	$\mathbf{8.65 \times 10^{-5}}$	$\mathbf{2.99 \times 10^{-5}}$
	RseR (t)	**33.57**	**33.87**	**33.723**	**31.31**
	$\varepsilon_{t,\text{RseR}}$ **(μstrains)**	**273.39**	**299.81**	**322.78**	**287.18**
Criterion 2	**K**	**16,000**	**16,000**	**16,000**	**16,000**
Vertical strains at the top of UGM	Peak 1	**423**	**419**	**427**	**412**
	Trough 1	200	100	80	85
	Peak 2	**423**	**419**	**427**	**412**
	ΔD	$\mathbf{1.56 \times 10^{-7}}$	$\mathbf{1.52 \times 10^{-7}}$	$\mathbf{1.66 \times 10^{-7}}$	$\mathbf{1.41 \times 10^{-7}}$
Criterion 2	**K**	**16,000**	**16,000**	**16,000**	**16,000**
Vertical strains at the top of the subgrade	Peak 1	**976**	**867**	**894**	**724**
	Trough 1	550	700	600	415
	Peak 2	**976**	**867**	**894**	**724**
	ΔD	$\mathbf{6.58 \times 10^{-6}}$	$\mathbf{3.25 \times 10^{-6}}$	$\mathbf{4.23 \times 10^{-6}}$	$\mathbf{1.71 \times 10^{-6}}$

the number of maximum axles loads allowed for a bogie of A340, B77, and A380 before the failure of the layers.

6 Conclusion

In this study, flexible pavement structures with platforms A, B, C, and D, respectively, recommended by ICAO were modelled under static loading of bogies from heavy weight A340, B777, and A380 aircrafts. Initially, the mechanical deflections, stresses, and strains in the said pavements were determined by the 3D numerical modelling from Cast3M FE calculation code. From the results of these computations, it appears that these structures A, B, C, and D recommended by ICAO are not equivalent from the point of view of mechanical behaviour as claimed by the empirical method for the design of aeronautical bituminous pavements with abacus. The representation of the strain shapes was done with 3D and 2D profiles to improve the quality of response and to clearly identify the critical areas when passing an aircraft bogie. From an aircraft point of view, the four- and six-wheels bogies of the A380 are more destructive to flexible pavements than the bogies of the other aircrafts tested in this study. The calculation of damage according to the new French rational method for aeronautical flexible pavements revealed that the main damage to these pavements is due to the fatigue of the

Table 9: Summary of maximum elementary damage in the airfield pavement structures

Trend analysis of elementary damage ΔD and number of total axles N_i on flexible pavements				
Aircraft	**CBR = 3**	**CBR = 6**	**CBR = 10**	**CBR = 15**
A340	$\Delta D = 5.83 \times 10^{-5}$ and $N_0 = 17{,}153$	$\Delta D = \mathbf{9.24 \times 10^{-5}}$ and $N_0 = 10{,}823$	$\Delta D = 8.65 \times 10^{-5}$ and $N_0 = 11{,}561$	$\Delta D = 2.99 \times 10^{-5}$ and $N_0 = 33{,}445$
B777	$\Delta D = 6.92 \times 10^{-4}$ and $N_1 = 1{,}445$	$\Delta D = 5.99 \times 10^{-4}$ and $N_1 = 1{,}669$	$\Delta D = \mathbf{7.09 \times 10^{-4}}$ and $N_1 = 1{,}410$	$\Delta D = 3.44 \times 10^{-4}$ and $N_1 = 2{,}907$
A380-C7	$\Delta D = 1.71 \times 10^{-3}$ and $N_2 = 585$	$\Delta D = 2.60 \times 10^{-3}$ and $N_2 = 385$	$\Delta D = \mathbf{2.72 \times 10^{-3}}$ and $N_2 = 368$	$\Delta D = 9.32 \times 10^{-4}$ and $N_2 = 1{,}073$
ΔD (A380-C7)/ΔD (B777)	2.47	4.34	3.83	2.71
ΔD (A380-C7)/ΔD (A340)	29.34	28.14	31.39	31.12

bituminous layers and not to the bearing or rutting of the platform/subgrade and the UGM layers as recommended by the empirical design method of aeronautical flexible pavements with abacus. Being aware that there cannot be only one type of aircraft on such airfield pavement, a damage formula derived from Miner's Law has been proposed in order to take into account the mix of traffic on the airfield pavement. This study proposes a state-of-the-art process to compute damage of flexible airfield pavement from new French rational method depending on the special technical clauses.

Funding information: The authors state no funding involved.

Author contributions: All authors have accepted responsibility for the entire content of this manuscript and consented to its submission to the journal, reviewed all the results, and approved the final version of the manuscript. The numerical modelling of the pavements was carried out by ZA. The analyse and interpretation of the results following the state-of-the-art were carried out by ZA and OOCF. The writing and formatting of the manuscript were performed by ZA and OOCF.

Conflict of interest: Authors state no conflict of interest.

Data availability statement: The data used to support the findings of this study are included within the article.

References

[1] Ambassa Z, Eko RM. Numerical analysis of flexible airfield pavement behavior submitted by large aircraft: Influence of the position and configuration of the landing gear. Mater Compon Sci. 2024 in Press.

[2] Priyanka S, Tutumluer E. Airfield pavement damage evaluation due to new-generation aircraft wheel loading and wander patterns. J Transp Res Board. 2018;2672(29):1–11. doi: 10.1177/0361198118799705.

[3] Wei B, Guo C. Predicting the remaining service life of civil airport runway considerating reliability and damage accumulation. Adv Mater Sci Eng J, Hindawi. 2022;2022:1–11. doi: 10.1155/2022/6494812.

[4] DGAC-STBA. Dimensionnement des chaussées-Instruction sur le dimensionnement des chaussées d'aérodromes et la détermination des charges admissibles. France: STBA, janvier; 1988. p. 84.

[5] Kerzrého J-P, Hornych P, Chabot A, Trichet S, Gouy T, Coirier G, et al. Evaluation of the aggressiveness of different multi-axle loads using APT. International Conference on APT, Nantes, France. p. 505–17.

[6] Broutin M. Assessment of flexible airfield pavements using Heavy Weight Deflectometers-Development of a FEM dynamical time-domain analysis for the backcalculation of structural properties. Doctor of Philosophy, ENPC, France; 2010. p. 370.

[7] Homsi F, Bodin D, Yotte S, Breysse D, Balay J-M. Multiple axle loadings: Shape parameters and their effect on the fatigue life of asphalt mixtures. Eur J Environ Civ Eng. 2011(15):743–58.

[8] ICAO. Design manual for runway. France: ICAO; 2005. p. 164.

[9] Ambassa Z, Amba JC, Tamaskovic N. Implementation of the c-phi reduction procedure in Cast3M code for calculating the stability of retaining walls in the layered backfill with strength parameters reduction by elasto-plastic finite element analysis using field data. Comptes Rendus Mécanique. 2023;2023:39.

[10] Zienkiewicz OC, Valliappan S, King IP. Elasto-plastic solution of engineering problems, Initial stress, finite element approach. Int J Numer Methods Eng. 1969;1:75–100.

[11] Zienkiewicz O, Taylor RL, Zhu JZ. The finite element method: its basis and fundamentals. London: Elsevier; 2005.

[12] PEP. Pavement experimental program of Airbus 380. France: LCPC-Airbus-STAC; 2001. p. 178.

[13] HTPT. High tire pressure test-technical report. France: DGAC-STAC-Airbus; 2010. p. 120.

[14] FCAA. Rational design method for flexible airfield pavements. Technical guide, French civil aviation authority. France: Civil aviation technical center; 2016. p. 138.

[15] Cast3M©. Cast3M is a research FEM environment; its development is sponsored by the French Atomic Energy Commission. Paris, France: French Atomic Energy Commission; 2022.

[16] Ambassa Z, Amba JC. Towards an advanced new emerging method of determination of Mohr-Coulomb parameters of soils from at the oedometric test: case study-Lateritic soils of Cameroon. Hindawi: Math Probl Eng. 2022;2022:18. doi: 10.1155/2022/4222654.

[17] Ambassa Z, Amba JC. Assessment of stiffness and strength parameters for the soft soil model of clays of Cameroon. Hindawi, Int J Adv Civ Eng. 2020;1:1–16.

[18] GAN. Guide d'application des normes-Enrobés hydrocarbonés et enduits superficiels pour chaussées aéronautiques. France: DGAC-STBA; 2012. p. 78.

[19] GTR. Guide des Terrassements Routiers, réalisation de remblais et des couches de forme, fascicules I et II, SETRA-LCPC, 2è édition. New York, USA: Prentice Hall; 2000. p. 211.

[20] Huang YH. Pavement analysis and design. USA: Pearson Prentice Hall; 2004.

[21] Burmister DM. The theory of stresses and displacements in layered systems and applications of the design of airport runways. Proceeding of the Highway Research Board. Vol. 23, 1943. p. 126–48.

[22] Dhatt G, Touzot G. Une présentation de la méthode des éléments finis. Les presses de l'université Laval-Québec, Maloine S.A. Editeur Paris, France; 1981. p. 134–5.

[23] Tornabene F, Viscoti M, Dimitri R. Thermo-mechanical analysis of laminated doubly-curved shells: higher order Equivalent Layer-Wise formulation. Compos Struct. 2024;335:117995.

[24] Tornabene F, Brischetto S. 3D capability of refined GDQ models for the bending analysis of composite and sandwich plates, spherical and doubly-curved shells. Thin-Walled Struct. 2018;129:94–124.

[25] Chatti K, Salama HK. Evaluation of fatigue and rut damage prediction methods for asphalt concrete pavements subjected to multiple axle loads. Int J Pavement Eng. 2011;12(1):25–36.

[26] Chatti K, Manik A, Salama HK, Chadi M, Lee S. Effect of Michigan multi-axle trucks on pavement distress. Final Report MDOT. USA: Michigan Department of Transportation; 2009. p. 312.

[27] Salama HK, Chatti K. A laboratory investigation of the effect of multiple axle and truck configurations on HMA mixture rutting. Proceeding of the 7th International RILEM Symposium on Advanced Characterisation of Pavement and Soils Engineering Materials, (ACPSEM07). Vol. 2, Athens; June 2007. p. 1305–14.

[28] Chabot A, Chupin O, Deloffre L, Duhamel D. ViscoRoute 2.0 – A tool for the simulation of moving loads effects on asphalt pavement. Road Mater Pavement Des. 2010;11(2):227–50.

[29] Ambassa Z, Allou F, Petit C, Medjo R. Top-down and bottom-up fatigue cracking of bituminous pavement subjected to tangential moving loads. Proceedings of the 7th RILEM International Conference on Cracking in Pavement. Vol. 4, The Netherlands; 2012. p. 675–85.

[30] Ambassa Z, Allou F, Petit C, Medjo R. Fatigue Life prediction of an asphalt pavement subjected to multiple axle loadings with viscoelastic FEM. Int J Constr Build Mater. 2013;43:443–52.

[31] Afnor. Dimensionnement structurel des chaussées routières – Application aux chaussées neuves. NF P98-086, Mai; 2019.

[32] White G. Limitations and potential improvement of the aircraft pavement strength rating system to protect airport asphalt surfaces. Int J Pavement Eng. 2017;18(12):1111–21.

[33] Baoli W, Chengchao G. Predicting the remaining service life of civil airport runway considering reliability and damage accumulation. Adv Mater Sci Eng. 2022;2022(1):6494812.

[34] Wesolowski M, Blacha K, Iwanowski P. Complex method of airfield pavement condition evaluation based on APCI index. MDPI, Appl Sci J. 2022;12:21.

[35] Miner MA. Cumulative damage in fatigue. J Appl Mech. 1945;1:159–64.